

# Sophistications of cell sorting

Jeremy B.A. Green

**The self-sorting of early embryonic cells is mediated not only by pure differential adhesion but also involves other processes. Direct force measurements reveal the role of cell-cortical tension, whereas epithelial-wrapping dominates the sorting of enclosed mesenchymal cells.**

Everyone knows that oil and water do not mix. More interestingly, when shaken together, oil and water self-organize into two layers. In 1955, Townes and Holtfreter famously demonstrated a similar 'unmixing' when cells from the three germ layers of the early vertebrate embryo were combined<sup>1</sup>. They hypothesized that embryos rely on differential cell 'affinity' to organize these layers during normal development<sup>1,2</sup>. Using similar assays (Fig. 1), Steinberg proposed that the forces organizing the cells are closely analogous to those organizing the molecules of immiscible fluids<sup>3</sup> and put forward the Differential Adhesion Hypothesis (DAH): in engulfment and unmixing assays of two cell populations, the more cohesive one (with the stronger cell-cell, or homotypic, adhesion) would distribute in the middle and the less cohesive one on the outside. Differential expression of the cell adhesion molecule cadherin is sufficient to drive cell sorting<sup>4</sup>, exactly as predicted by the model<sup>5</sup>. However, to some the DAH was only one of the possible mechanisms and, despite acceptance as the conventional wisdom, DAH has remained controversial<sup>6</sup>. In a lucid critique of Steinberg, Harris proposed a Differential Surface Contraction (DSC) model in which cortical tension (the force generated within cells parallel to their surface) rather than adhesion between cells *per se*, could drive cell sorting<sup>7</sup>.

On page 429 of this issue, Krieg *et al.*<sup>8</sup> tested these two models by directly measuring the adhesiveness and cortical tension of cells from the three germ layers of zebrafish embryos using an atomic force microscope — a tiny probe mounted and calibrated so that its bending by an object at its tip can be measured and the corresponding bending force determined (Fig. 2). They measured cell adhesion by attaching one cell to the end of the microscope probe and a second cell to a fixed substrate below, bringing the two cells together and monitoring the force required to pull them apart. They

also determined cortical tension by measuring the force needed for a hard bead attached to the end of the probe to deform the surface of a cell attached to the surface below. Measurements for cells from the ectoderm (Ec), mesoderm (M) and endoderm (En) showed that homotypic adhesion was stronger in mesoderm than in ectoderm, whereas endoderm values were in between ( $AdM > AdEn > AdEc$ ). As expected, adhesion was calcium-dependent and correlated with cadherin expression at the surface. The hierarchy of cortical tension values was different:  $CtEc > CtM > CtEn$ . In pairwise sorting assays, ectoderm cells were always in the middle, opposite to what would be predicted by DAH, under which their low homotypic adhesion would place them on the outside. The central position of ectoderm cells within the aggregates correlated instead with higher cortical tension. Mesoderm cells were also surrounded by endoderm, extending the correlation. This would seem to be a triumph of DSC (and similar models<sup>6</sup>) over DAH, at least for

these cell types, although it fails to reproduce the *in vivo* configuration (ectoderm outside and endoderm innermost) and mechanisms involving differential adhesion and cortical tension are not mutually exclusive.

Apart from requiring a change in what textbooks say about the importance of differential adhesion in cell self-sorting, the work of Krieg *et al.* leads us to reconsider the role of different cell-biological processes in self-sorting. For a start, the cortical actomyosin cytoskeleton becomes more significant. Krieg *et al.* showed that disruption of this network, using blebbistatin (an inhibitor of myosin II activity) and dominant-negative Rho kinase, blocks cell self-sorting. This suggests that sorting is more akin to active migration, in which changes in cell shape are crucial, whereas according to the DAH, cells are, effectively, structureless units. It is no surprise, then, that integrins, adhesion molecules associated with migration, can be crucial for cell sorting<sup>9</sup>. There are also instances when  $\beta$ -catenin regulation

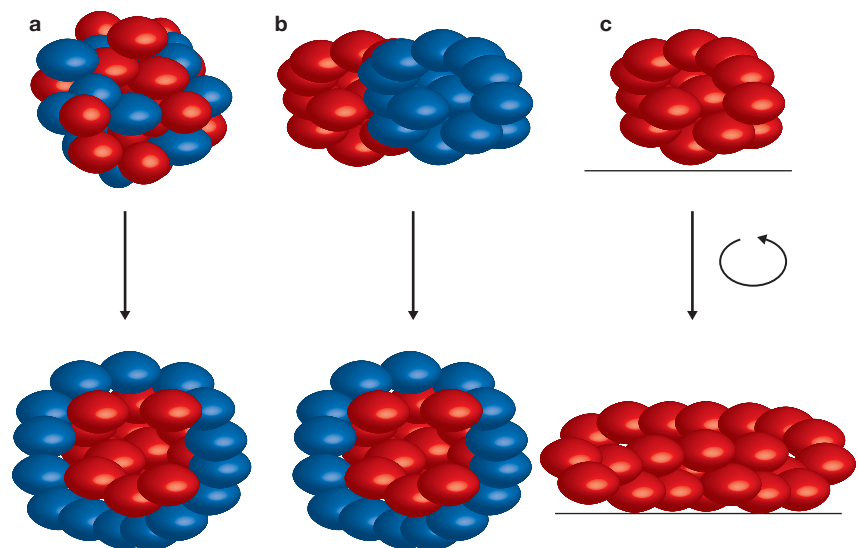


**Figure 1** Classical assays for cell sorting and apparent surface tension. (a) Cell aggregates made up from two different cell types unmix (self-sort) concentrically. (b) Aggregates of two different cell types are juxtaposed and one engulfs the other. (c) Cell aggregates of a single type are centrifuged to flatten them and the deformation they undergo provides a measure of apparent aggregate surface tension (summed homotypic cell adhesion and/or cell-cortical tension).

Jeremy B. A. Green is in the Department of Craniofacial Development, King's College, London, SE1 9RT, UK.  
e-mail: Jeremy.green@kcl.ac.uk

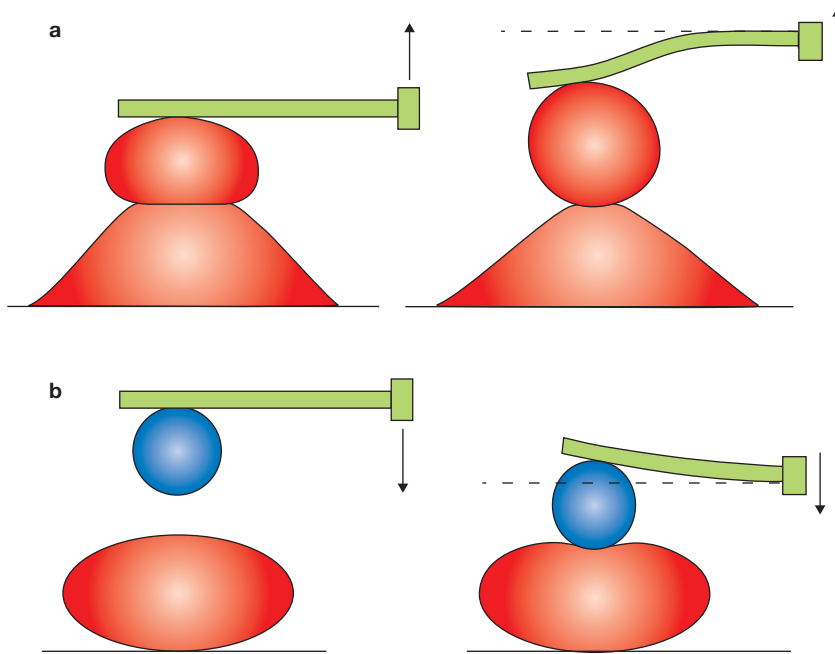


**Figure 2** Direct measurement of cell adhesion and cell deformability with an atomic force microscope. (a) A cell attached to a probe with Concavalin A is brought in contact with a cell similarly attached to a substrate. The force required to pull cells apart is measured as a function of the deformation of the probe (detected by the angle of deflection of a laser beam, data not shown) and reflects the strength of cell–cell adhesion. (b) A hard bead (blue) attached to a probe is slowly brought down onto the surface of a cell until the latter is deformed. Deformation by the probe measures the resistive force, which is a function of the cell-cortical tension.

of cadherin, the adhesion molecule traditionally thought to account for self-sorting is, at most, secondary<sup>10</sup>. Second, the DSC model predicts that contractility must be different and higher at cell-medium interfaces than at internal interfaces<sup>7</sup>. In other words, cortical tension should be localized by cell polarization. Krieg *et al.* addressed this prediction in two ways. First, using computer models of cell sorting with and without localization of cortical tension, they found that sorting operates only when the cortical tension is localized. Second, by examining actin in real-cell aggregates, they showed that it was enriched at the cell-medium interface; however, they did not look at heterotypic cell interfaces, which would have been a useful addition.

Townes and Holfreter<sup>1</sup> had already hinted at the importance of active cell-surface contraction for self-sorting, when they noticed that neurectodermal cells, whether as single cells or organized as sheets, were engulfed by endodermal cells. Neurectodermal sheets penetrated an endodermal mass by infolding or invagination, recapitulating the rolling-up neurulation movements that make a tubular spinal cord. They proposed that the same mechanism may drive both invagination and cell sorting.

Indeed, actomyosin-driven apical contraction is now recognized as the main mechanism of epithelial folding in the neural plate and elsewhere, and support for actomyosin-dependent DSC provides a mechanistic link between cell self-sorting and epithelial folding.

Despite the support Krieg *et al.* provide for the DSC hypothesis, how can one explain the peculiar inside-out arrangement observed by the authors in their *in vitro* experiments, in which the ectoderm or the mesoderm are inside the aggregates (one does not need to know much about developmental biology, but merely a little Greek, to know that ectoderm should be on the outside and endoderm on the inside of embryos, with mesoderm in the middle)? To address this issue, the authors attempted to assay cell self-sorting '*in vivo*' using transplantation experiments. They conclude that strong interactions of germ-layer cells with the yolk and the enveloping layer cells invert the inside-out cell sorting seen *in vitro*, thereby producing the endo-in/ecto-out arrangement that we and the fish prefer. Whether this zebrafish-specific dominance of yolk and enveloping-layer cell interactions significantly undermines the authors' case for DSC remains to be seen. Moreover, other challenges should be addressed before applying these

findings *in vivo*, when one considers that: first, the quality and strength of adhesions change with contact time (a factor barely taken into account in the authors' adhesion assays); second, cortical tension is only one of several factors determining cell deformability; third, mesodermal cells in zebrafish move as a loose population; fourth, the authors examined the actin distribution at late-differentiating stages rather than during sorting; fifth, that adhesion of sheets of cells may be different from that of individual cells. Krieg *et al.* make a respectable effort, but there remains the inevitable compromise between beautiful measurements on few cells and biological relevance of messy tissues that is the cell biologist's Uncertainty Principle.

This brings us to a recent article by Ninomiya and Winklbauer<sup>11</sup>, which extends their previous finding that tissue elongation in mesodermal explants and cell aggregates is enhanced by a wrapping of epithelium<sup>12</sup>. Although quite dramatic elongation is possible without it<sup>13</sup>, tissue elongation within an epithelial wrapping occurs normally during development and, of course, contrasts with the rounding-up of cell aggregates *in vitro*. Ninomiya and Winklbauer showed that epithelial wrapping not only enhanced elongation of mesodermal tissue but also increased the centrifugation-induced flattening of rounded-up ectodermal cell aggregates and modified the concentric engulfment and self-sorting of mixed cell types to give a linear arrangement of tissues. They explain their observations as a reduction in surface tension of the aggregates by adhesion to the epithelium. Forces along the surface of cell aggregates resemble fluid surface tension and can be modelled as such, whether driven by adhesion (as with molecules in fluids, and as in DAH) or by cortical tension (as in DSC). However, the DAH-flavoured terminology used by Ninomiya and Winklbauer is secondary to the observation that the epithelium is important and presumably facilitates tissue elongation by reducing the tensions (whether intracellular or intercellular) that drive concentric cell self-sorting and aggregate rounding. Of course, epithelial signalling and polarization of mesenchymal migratory behaviour may also be involved.

In a further instance of how an epithelium breaks the usual sorting rules, Ninomiya and Winklbauer prepared aggregates, in which untreated ectodermal cells were mixed with similar cells, and in which they expressed M-PAPC, a paraxial protocadherin derivative that reduces

cadherin-dependent adhesion<sup>14</sup>. As expected, M-PAPC-expressing cells, with their reduced cohesion, sorted to the outside. Unexpectedly, wrapping with normal epithelial ectoderm sent M-PAPC-expressing cells to the inside, whereas wrapping with M-PAPC-expressing ectoderm kept them on the outside. In short, cells with the same M-PAPC status stick together, suggesting that more complex cell interactions may influence the result of these experiments<sup>15</sup>.

The exciting aspect of these papers is that, building on the brilliance of Holtfreter,

Steinberg, Harris and others, they represent a new chapter in the analysis of morphogenesis, in which high-resolution force measurement and molecular analysis will be combined with more physiological and multi-component models. Thanks to this type of analysis, the complexity of real embryos is gradually coming within the grasp of hardcore cell biology.

1. Townes, P. L. & Holtfreter, J. *J. Exp. Zool.* **128**, 53–120 (1955).
2. Steinberg, M. S. & Gilbert, S. F. *J. Exp. Zool.* **301**, 701–706 (2004).
3. Steinberg, M. S. *Curr. Opin. Dev.* **17**, 281–286 (2007).

4. Foty, R. A. & Steinberg, M. S. *Dev. Biol.* **278**, 255–263 (2005).
5. Steinberg, M. S. *J. Exp. Zool.* **173**, 395–443 (1970).
6. Brodland, G. W. *Appl. Mech. Rev.* **57**, 47–76 (2004).
7. Harris, A. K. *J. Theoret. Biol.* **61**, 267–285 (1976).
8. Krieg, M. *et al. Nature Cell Biol.* **10**, 429–436 (2008).
9. Marsden, M. & DeSimone, D. W. *Curr. Biol.* **13**, 1182–1191 (2003).
10. Reintsch, W. E. *et al. J. Cell Biol.* **170**, 675–686 (2005).
11. Ninomiya, H. & Winklbauer, R. *Nature Cell Biol.* **10**, 61–69 (2008).
12. Ninomiya, H., Elinson, R. P. & Winklbauer, R. *Nature* **430**, 364–367 (2004).
13. Green, J. B., Dominguez, I. & Davidson, L. A. *Dev. Dyn.* **231**, 576–581 (2004).
14. Chen, X. & Gumbiner, B. M. *J. Cell Biol.* **174**, 301–313 (2006).
15. Davidson, L. A. *Dev. Cell* **14**, 152–154 (2008).

## BRCA1 and stem cells: tumour typecasting

Matthew J. Smalley, Jorge S. Reis-Filho and Alan Ashworth

**Phenotypic variation between tumour types is likely to reflect the nature of the cell of origin and the genes involved in pathogenesis. Compared with most sporadic breast cancers, those arising in carriers of *BRCA1* mutations usually have distinctive pathological characteristics. A new study suggests that a role for *BRCA1* in the determination of stem-cell fate may explain this phenomenon.**

The ducts and lobules of the human breast are made up of two morphologically distinct cell populations: the inner, milk producing luminal epithelial cells, which express low molecular-weight cytokeratins and the oestrogen receptor (ER), and the outer, supporting basal myoepithelial cells, which express high molecular-weight cytokeratins and smooth muscle markers<sup>1</sup>. There is considerable evidence for a differentiation hierarchy within the breast (Fig. 1) and a common cell of origin of luminal and myoepithelial cells — a mammary stem cell. Similar to the differentiated myoepithelial cells, the stem cell is thought to have a basal phenotype<sup>1,2</sup>. Tumours arising in carriers of germ-line mutations in the breast cancer susceptibility gene *BRCA1* are commonly of the basal subtype, whereas sporadic cases are much more likely to be luminal in nature<sup>2</sup>. Because of this, it has been suggested previously that *BRCA1* may be a stem-cell regulator<sup>3</sup> and that basal-like carcinomas originate from stem cells

that have a block in differentiation<sup>4</sup>. Wicha and colleagues now provide support for this notion by showing that loss of *BRCA1* may limit the differentiation potential of mammary stem/progenitor cells, thus preventing formation of ER-positive luminal epithelial cells<sup>5</sup>.

Germline *BRCA1* gene mutations cause a significantly increased risk of breast and ovarian cancer. *BRCA1* has been implicated in a plethora of cellular processes, including the response to DNA damage, X-chromosome inactivation, ubiquitination and chromatin remodelling<sup>6</sup>. Furthermore, a number of lines of evidence indicate that *BRCA1* functions in the regulation of transcription; indeed, *BRCA1* seems to regulate the expression of ER  $\alpha$  directly<sup>7</sup>. This is consistent with the clinical observation that most cancers developing in carriers of *BRCA1* mutations have an ER-negative basal-like phenotype<sup>2,8</sup>. Moreover, it has been suggested that these tumours may recapitulate some features of breast stem cells<sup>2,8</sup>. However, a causal relationship between *BRCA1* dysfunction and the basal-like phenotype remains to be demonstrated, and whether *BRCA1* inactivation blocks the differentiation of stem cells or leads to the re-acquisition of stem-cell-like properties has so far been a matter of contention.

Wicha and colleagues used a number of approaches to investigate how *BRCA1* may be involved in stem-cell regulation or lineage determination<sup>5</sup>. First, they noted that *BRCA1* levels were elevated in mammary cells that were cultured *in vitro* as mammospheres (balls of undifferentiated mammary epithelial cells grown in suspension culture, which can be serially passaged into secondary and tertiary spheres). There is good evidence that only mammary stem cells can generate these structures and that they are composed of both undifferentiated stem and early progenitor cells<sup>9</sup>. Although knockdown of *BRCA1* expression, mediated by RNA interference (RNAi), had no effect on primary mammosphere formation, passaging was severely affected. An assay for stem cells using the Aldefluor stain, which is cleaved by the breast stem-cell marker ALDH1 to generate a fluorescent product<sup>9</sup>, indicated that the number of such cells was increased. This was interpreted as an indication that *BRCA1* may be involved in mammary stem-cell self-renewal but not progenitor-cell proliferation. Furthermore, RNAi-mediated *BRCA1* knockdown resulted in a 10-fold reduction in cells expressing ER and an increase in the number of cells with

Matthew J. Smalley, Jorge S. Reis-Filho and Alan Ashworth are at The Breakthrough Breast Cancer Research Centre, The Institute of Cancer Research, Fulham Road, London, SW3 6JB, UK. e-mail Alan.Ashworth@icr.ac.uk; Matthew.Smalley@icr.ac.uk; Jorge.Reis-Filho@icr.ac.uk

# Tensile forces govern germ-layer organization in zebrafish

M. Krieg<sup>1</sup>, Y. Arboleda-Estudillo<sup>1,2</sup>, P.-H. Puech<sup>3</sup>, J. Käfer<sup>4</sup>, F. Graner<sup>4</sup>, D. J. Müller<sup>1,5</sup> and C.-P. Heisenberg<sup>2,5</sup>

**Understanding the factors that direct tissue organization during development is one of the most fundamental goals in developmental biology. Various hypotheses explain cell sorting and tissue organization on the basis of the adhesive and mechanical properties of the constituent cells<sup>1</sup>. However, validating these hypotheses has been difficult due to the lack of appropriate tools to measure these parameters. Here we use atomic force microscopy (AFM) to quantify the adhesive and mechanical properties of individual ectoderm, mesoderm and endoderm progenitor cells from gastrulating zebrafish embryos. Combining these data with tissue self-assembly *in vitro* and the sorting behaviour of progenitors *in vivo*, we have shown that differential actomyosin-dependent cell-cortex tension, regulated by Nodal/TGF $\beta$ -signalling (transforming growth factor  $\beta$ ), constitutes a key factor that directs progenitor-cell sorting. These results demonstrate a previously unrecognized role for Nodal-controlled cell-cortex tension in germ-layer organization during gastrulation.**

Gastrulation is the first stage in vertebrate development when different progenitor types sort-out and assemble into distinct germ layers<sup>2</sup>. Both cell adhesion and contraction have long been implicated in germ-layer formation; however, their relative contribution to these processes is still a matter of debate<sup>3</sup>. We therefore sought to quantify the specific adhesive and mechanical properties of the different progenitor types at the single-cell level and correlate these values to the actual sorting behaviour of progenitors *in vitro* and *in vivo* (for generation of different germ-layer progenitor types see Supplementary Information, Fig. S1 and Methods).

To measure cell adhesion at the single-cell level, we used an atomic force microscope (AFM) as a single-cell force spectroscopy (SCFS; Fig. 1a; refs 4–6). Adhesion forces between two isolated zebrafish germ-layer cells were measured by bringing the cells into contact until a pre-defined force was reached and then recording the force needed to separate them after a given dwell-time, which ranged from 1–60 s. When adhesion forces between progenitors of the same type (homotypic adhesion; ‘cohesion’) were measured, ectoderm progenitors showed significantly less cohesion compared with their mesoderm and endoderm counterparts for all contact times tested (Fig. 1b; Supplementary

Information, Table S1, Fig. S2a, b). Adhesive forces between different progenitor types (heterotypic adhesion) were similar to homotypic cell contacts of ectoderm cells, the least cohesive cell type (Fig. 1c). The recorded differences in cell–cell adhesion are unlikely to be a consequence of dissimilar morphological and/or mechanical cell-properties, as neither cell size (Supplementary Information, Fig. S2c) nor ‘contact stiffness’ correlated with the recorded maximum adhesion forces ( $r = 0.14$ , Fig. 1d; see also Methods). Taken together, these observations demonstrate that mesoderm and endoderm progenitors are more cohesive than ectoderm cells.

Cadherin adhesion molecules, particularly E-cadherin, are known to have key roles in tissue morphogenesis during vertebrate gastrulation<sup>7</sup>. To test whether E-cadherin is involved in differential cohesion of germ-layer progenitors, we measured cohesion when E-cadherin function was impaired. Cohesion of all three progenitor types was markedly reduced when calcium ions were depleted from the medium and, more specifically, when E-cadherin expression was knocked down using morpholino antisense oligonucleotides (Fig. 1e), indicating that E-cadherin mediates progenitor-cell cohesion. To test whether the progenitors show differences in cadherin-mediated adhesion that are similar to their differential cohesive properties, we measured the adhesion of ectoderm, mesoderm and endoderm progenitors to substrates coated with E-cadherin<sup>8</sup>. Mesoderm and endoderm progenitors adhered more to E-cadherin substrates than ectoderm cells (Supplementary Information, Fig. S2d), indicating that adhesion of progenitors to cadherins correlates with their cohesive properties. Consistently, we found that in embryos at the onset of gastrulation (6 h post fertilization; hpf), E-cadherin density at the plasma membrane of mesendoderm (mesoderm and endoderm) progenitors was higher than in the directly adjacent ectoderm progenitors (Fig. 1f; Supplementary Information, Fig. S2e; ref. 9). Similarly, the amount of classical cadherins at the plasma membrane of dissociated ectoderm progenitors, detected by an anti-pan-cadherin antibody<sup>10</sup> on western blots, was lower than in mesoderm and endoderm cells (Fig. 1f’). Together, these findings demonstrate that differential cohesion of germ-layer progenitors is mediated primarily by classical cadherins including E-cadherin.

In addition to differential adhesion, differential cell contraction has been implicated in cell sorting and tissue self-assembly<sup>11</sup>. Studies using

<sup>1</sup>BIOTEC, Technische Universität Dresden, Tatzberg 47-51, 01307 Dresden, Germany. <sup>2</sup>Max-Planck-Institute for Molecular Cell Biology and Genetics, Pfotenhauerstr. 108, 01307 Dresden, Germany. <sup>3</sup>INSERM/UMR 600, CNRS/UMR6212, Case 937, 163 Avenue de Luminy, 13288 Marseille, France. <sup>4</sup>Laboratoire de Spectrométrie Physique, UMR 5588, UJF Grenoble I & CNRS, 140 Avenue de la Physique, 38402 Saint Martin d’Hères, France.

<sup>5</sup>Correspondence should be addressed to C.-P.H or D.J.M. (e-mail: heisenberg@mpi-cbg.de; mueller@biotec.tu-dresden.de)

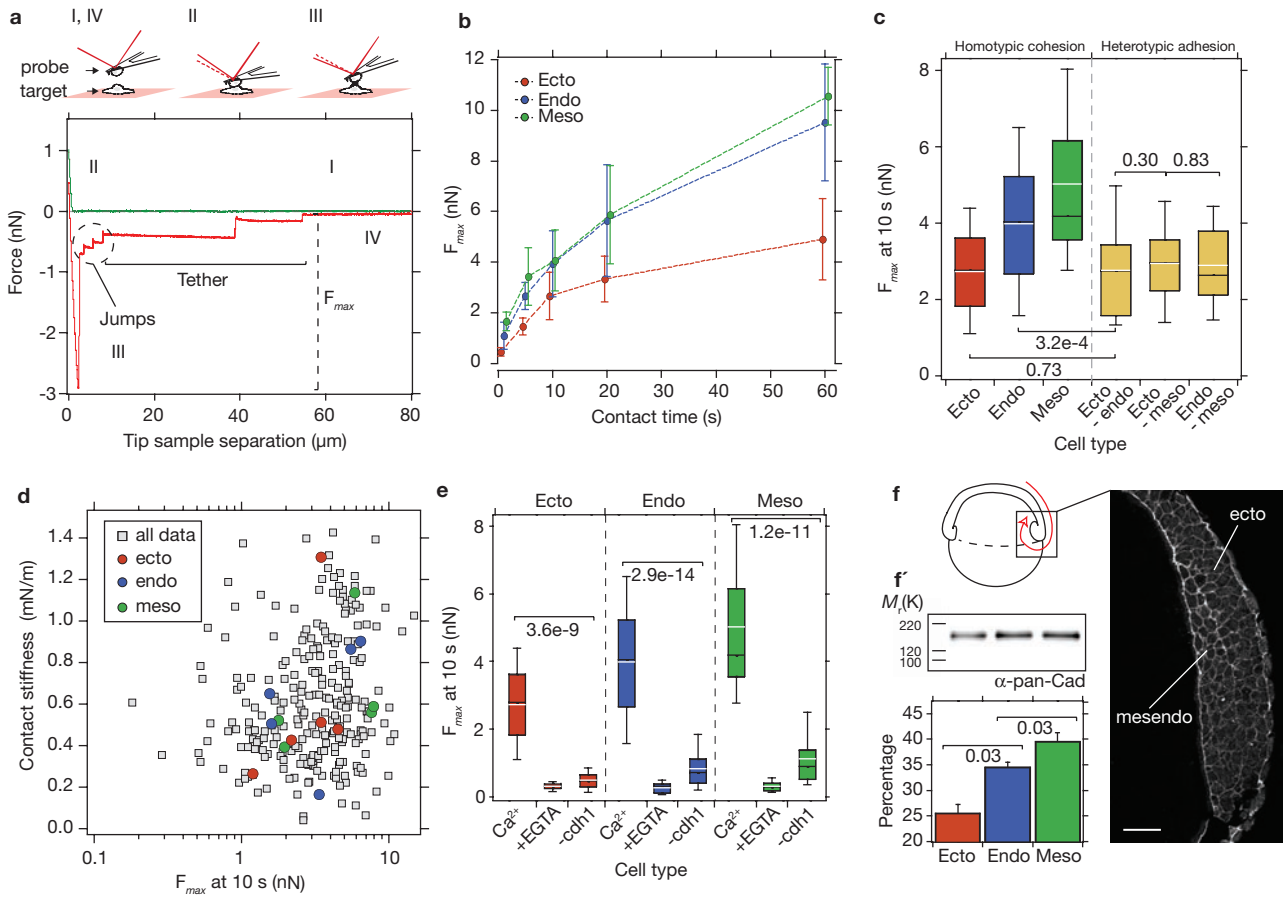


**Figure 1** Adhesion of germ-layer progenitors measured by single-cell force spectroscopy (SCFS). **(a)** Outline of the SCFS adhesion assay. One cell immobilized on an AFM cantilever (probe) is brought into contact at a given speed with a second cell adhering to a solid substrate (target). After a predefined contact time, the cell was retracted at the same speed and the interaction force was detected by the cantilever deflection. The resultant force-distance curve allows quantification of the maximum adhesion force ( $F_{max}$ ). **(b)**  $F_{max}$  as a function of contact time for homotypic adhesion between the three different progenitor types. Values are presented as median  $\pm$  MAD. For detailed representations of the statistics see Supplementary Information, Fig. S2a, b, Table S1. **(c)** Homotypic versus heterotypic progenitor adhesion at 10 s contact time. Data is presented as a box-whisker plot. Median is black and mean is white. **(d)** Slope of contact region ('contact stiffness') extracted

from the approach trace versus  $F_{max}$  recorded for each force-distance curve. Grey squares, no statistical correlation was seen ( $r = 0.14$ ); five arbitrarily chosen curves for each progenitor types are highlighted as coloured circles. **(e)**  $F_{max}$  for homotypic adhesion at 10 s contact in control ( $Ca^{2+}$ ), EGTA (5 mM)-treated or *E-cadherin*-morpholino oligonucleotide expressing ( $-cdh1$ ; 8 ng per embryo) progenitors. **(f)** Sagittal section of the dorsal germ-ring margin of a shield stage wild-type embryo (6 hpf; schematic drawing in upper left corner) fluorescently stained with an *E-cadherin* antibody. Picture was taken by confocal microscopy. **(f')** Western blot analysis and quantification (bar chart) of the amount of biotinylated, membrane-bound classical cadherins (pan-Cadherin antibody) in dissociated progenitors normalized to total tubulin ( $n = 4$ ; median  $\pm$  MAD). Scale bar in **(f)**, 50  $\mu m$ . Numbers above or below square brackets indicate *P* values for the corresponding combinations.

*Dictyostelium discoideum*, fibroblasts and white blood cells have shown that actomyosin contraction and cell-cortex tension are directly related to each other<sup>12–14</sup>. We therefore determined cell-cortex tension of different germ-layer progenitors as a read-out of their specific actomyosin activity. To measure cell-cortex tension, we deformed the surface of single progenitors with a colloidal force probe and recorded the resulting force-indentation curves with an AFM (Fig. 2a). Cell-cortex tension was extracted from force-indentation curves using the cortical shell-liquid core or liquid droplet model<sup>13</sup> (for details see Methods). We found that ectoderm progenitors had the highest cell-cortex tension, followed by mesoderm and then endoderm progenitors (Fig. 2b–d). To determine whether these differences in cell-cortex tensions were due to differential actomyosin activity, we measured cell-cortex tension of germ-layer progenitors in the presence of blebbistatin (see Methods for details), a specific inhibitor of myosin II activity. Exposure to blebbistatin reduced cell-cortex tension to the same level in all progenitor types (Fig. 2d).

Together, these findings demonstrate that progenitors show differential actomyosin-dependent cell-cortex tension.

The factors regulating cell-cortex tension of germ-layer progenitors are poorly understood. Nodal/TGF $\beta$  signalling is known to be required and sufficient to induce mesoderm and endoderm cell fates and morphogenesis<sup>15</sup>. Thus, to test whether Nodal/TGF $\beta$  signalling can modulate cell-cortex tension of progenitors, we measured cortex tension of ectoderm progenitors exposed to recombinant activin, a Nodal-related TGF $\beta$  signal previously shown to function as a mesendoderm inducer and dorsalizer<sup>16</sup>. In ectoderm progenitors cultured for 120 min in the presence of activin (100 ng ml<sup>-1</sup>), cell-cortex tension was significantly lower than in untreated cells (untreated =  $54.5 \pm 8.6 \mu N m^{-1}$ ,  $n = 32$ ; treated =  $21.7 \pm 8.6 \mu N m^{-1}$ ,  $n = 32$ ; median  $\pm$  MAD;  $P = 2.2 \times 10^{-16}$ ). This suggests that actomyosin-dependent cell-cortex tension of germ-layer progenitors can be modulated by Nodal/TGF $\beta$ -related signalling.

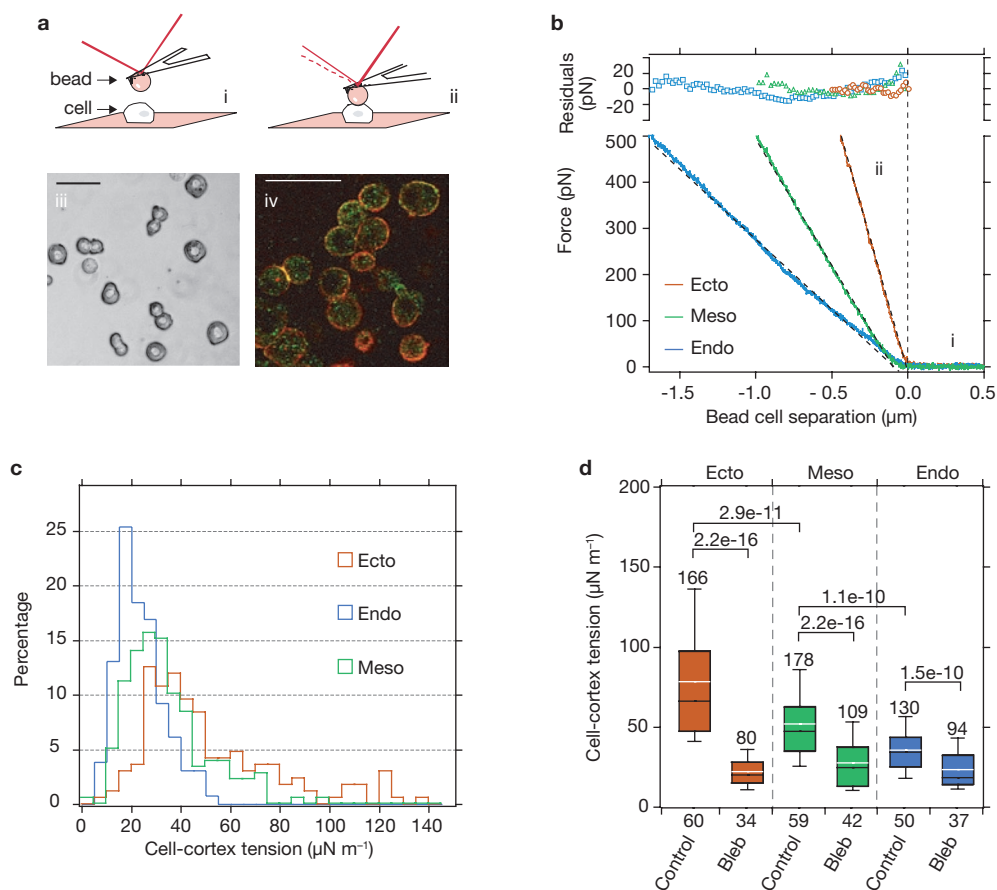


**Figure 2** Cell-cortex tension of germ-layer progenitors measured by SCFS. (a) Principle of the indentation experiment. A passivated colloidal force probe (bead; diameter = 5  $\mu\text{m}$ ) is moved towards a given progenitor cell (cell) at  $1 \mu\text{m s}^{-1}$  (i) and the cell surface is deformed by the bead (ii). (iii) Phase-contrast micrograph of typical progenitors used for measurements. (iv) Phalloidin (actin; red) and anti-phospho-myosin antibody (green) staining of fixed mesoderm progenitors after 3 h in culture. Scale bars in iii and iv, 50  $\mu\text{m}$ . (b) Representative force curves for progenitor cells

are shown and fitted to a linear model to extract the cell-cortex tension. The upper panel shows the residuals of the fit. (c) Distribution of cell-cortex tension for ectoderm, endoderm and mesoderm progenitors. (d) Box-whisker plot of cell-cortex tension for different progenitor cell types in the presence or absence of blebbistatin (bleb, 50  $\mu\text{M}$ ). Median is black and mean is white. Sample size is indicated over each box and number of tested cells below the x axis. Numbers above brackets indicate *P* values for the corresponding combinations.

To correlate our measurements of adhesion and cell-cortex tension with the actual sorting behaviour of germ-layer progenitors, we performed a series of *in vitro* cell sorting experiments (Fig. 3a). We have shown previously that ectoderm and mesoderm cells sort efficiently when mixed in primary culture, resulting in an ectoderm cluster surrounded by mesoderm cells<sup>17</sup>. Applying the same methodology to all three germ-layer progenitor types, we found that when ectoderm cells were mixed with either mesoderm or endoderm cells, ectoderm cell clusters became surrounded by mesoderm ( $n = 56$  aggregates) or endoderm cells ( $n = 45$ ) after 17 h in culture (Fig. 3b–f). Cell sorting also occurred in mixed mesoderm and endoderm cell populations after 17 h in culture with mesoderm clusters completely ( $n = 27$ ) or partially ( $n = 29$ ) enveloped by endoderm cells (Fig. 3g). Importantly, germ-layer progenitor aggregation began immediately after seeding and cell sorting was already evident minutes after mixing (Fig. 3h). This suggests that the cell–cell contact times used in our adhesion assay (Fig. 1b) are relevant for the actual sorting behaviour of progenitors. A sorting order of germ-layer progenitors thus exists *in vitro*; ectoderm cells are surrounded by mesoderm or endoderm cells and mesoderm cells are

surrounded by endoderm cells. Analogous configurations and sorting orders have been reported for dissociated germ-layer progenitors of *Rana pipiens* embryos<sup>18</sup>.

That higher actomyosin-dependent cell-cortex tension (Fig. 2b–d), but not cohesion (Fig. 1c), correlates with ectoderm progenitor sorting to the inside of a heterotypic aggregate (Fig. 3e, f), suggests that cell-cortex tension, rather than cohesion, promotes progenitor sorting to the inside. To test whether actomyosin-dependent cell-cortex tension is required for progenitor sorting, we exposed mixed ectoderm and mesoderm (or endoderm) progenitors to drugs that perturb actomyosin activity. We found that mixed ectoderm and mesoderm (as well as endoderm) progenitors failed to sort efficiently when exposed to cytochalasin D (an actin depolymerizer) or (–)-blebbistatin (an inhibitor of myosin II activity; Fig. 3i, j, l, m; Supplementary Information, Fig. S3c), but not to (+)-blebbistatin (an inactive enantiomer, Supplementary Information, Fig. S3a). Similarly, no sorting occurred in the presence of BDM, a myosin inhibitor (Supplementary Information, Fig. S3b). Importantly, relative differences in homotypic cell–cell adhesion between the different progenitor types remained unchanged in the

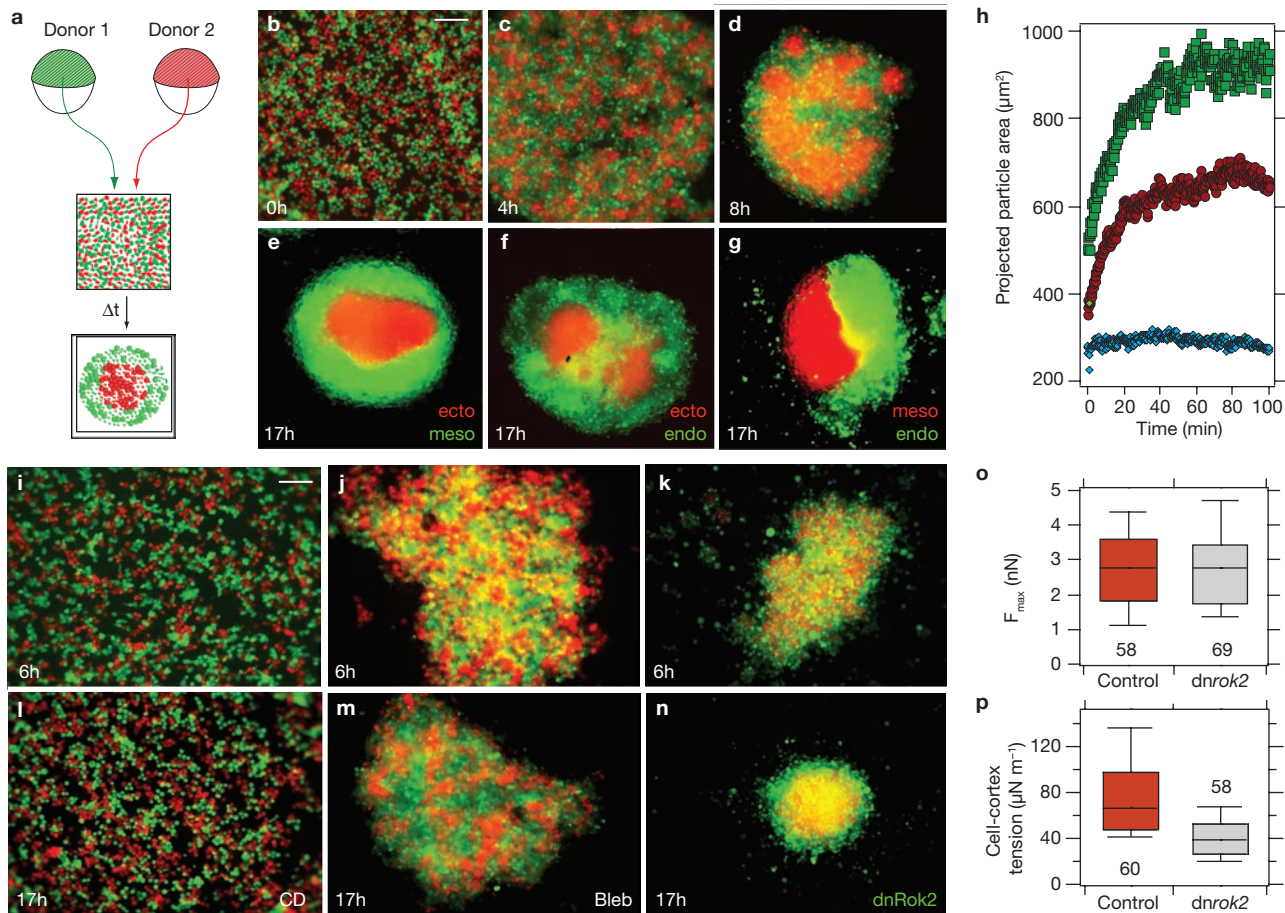


**Figure 3** Sorting of germ-layer progenitors *in vitro* (a) Schematic drawing of an *in vitro* progenitor cell sorting assay. Two different embryos were dissociated and progenitors were mixed in a hanging drop. Cell sorting was observed after 17 h in culture. (b–e) Sorting of mesoderm and ectoderm co-culture at different time-points. (f, g) Sorting of ectoderm-endoderm (f) and mesoderm-endoderm (g) co-cultures after 17 h in culture. (h) Time-course of cell sorting in an ectoderm-mesoderm co-culture. The cluster size (projected particle area) increased immediately after seeding without any detectable lag-phase (ectoderm, red circles; mesoderm, green squares), whereas no increase in cluster size was observed in the presence of EDTA (blue diamonds). Generally, progenitor cell aggregates after 17 h in culture did not show obvious signs of cell differentiation (as judged by marker

gene expression; data not shown; ref. 17), indicating that they retain their progenitor cell identities. (i, j, l, m) Hanging drop co-cultures of ectoderm (red) and mesoderm (green) progenitor cells in the presence of cytochalasin D (10 mM, i, l) or (–)-blebbistatin (50  $\mu$ M, j, m) after 6 h (i, j) and 17 h (l, m) in culture. (k, n) Hanging drop co-culture of untreated ectoderm cells and ectoderm cells obtained from embryos injected with 350 pg/embryo of *dnrok2* mRNA to reduce cortex tension after 6 h (k) and 17 h (n) in culture. (o) SCFS measurements of ectoderm cell cohesion (10 s contact time;  $P = 0.923$ ). (p) Cell-cortex tension in control and *dnrok2* mRNA expressing cells (350 pg/embryo;  $P = 2.2 \times 10^{-16}$ ). Number of tested cells are given below or above the boxes. Scale bars in (b, i), 300  $\mu$ m. Epifluorescence microscopy images were constructed in ImageJ.

presence of (–)-blebbistatin (Supplementary Information, Fig. S2f), indicating that blebbistatin functions in cell sorting by perturbing cell-cortex tension (Fig. 2d) rather than adhesion. Together, these findings show that differential actomyosin-dependent cell-cortex tension is required for efficient progenitor cell sorting.

To determine whether differential actomyosin-dependent cell-cortex tension is also sufficient to drive germ-layer progenitor cell sorting, we interfered selectively with actomyosin activation in ectoderm progenitors and then analysed their sorting behaviour when mixed with untreated ectoderm, mesoderm or endoderm cells. To cell-autonomously interfere with actomyosin activation, a dominant-negative version of Rho kinase 2 (*dnRok2*), an upstream regulator of actomyosin activity<sup>19</sup>, was expressed. *DnRok2*-expressing ectoderm progenitors showed reduced cell-cortex tension, whereas cohesion remained unchanged (Fig. 3o, p) and, when mixed with untreated ectoderm, mesoderm or endoderm cells,

sorted to the outside of heterotypic aggregates (Fig. 3k, n; Supplementary Information, Fig. S3d, f). Similar results were obtained by expressing a dominant-negative version of myosin regulatory light chain 2a (*dnMRLC2a*), a downstream target of *Rok2*, to reduce cortex tension (Supplementary Information, Fig. S3e). This suggests that differential actomyosin-dependent cell-cortex tension is sufficient to direct progenitor cell sorting.

To explain the sorting behaviour of germ-layer progenitors in the context of our adhesion and tension measurements, we simulated progenitor cell sorting using the Cellular Potts Model<sup>20,21</sup>. In this model, cell behaviour is driven by energy minimization whereby the total energy of an aggregate depends on the interfacial tension between cell-to-cell and cell-to-medium interfaces<sup>3,22</sup>. The interfacial tension between two cells is determined by the adhesion ( $J_{ij}$ ) between the cell types  $i$  and  $j$ , and by the cortex elasticity and cortex tension ( $T_i$  and  $T_j$ ) of the two cells<sup>3,23</sup>.

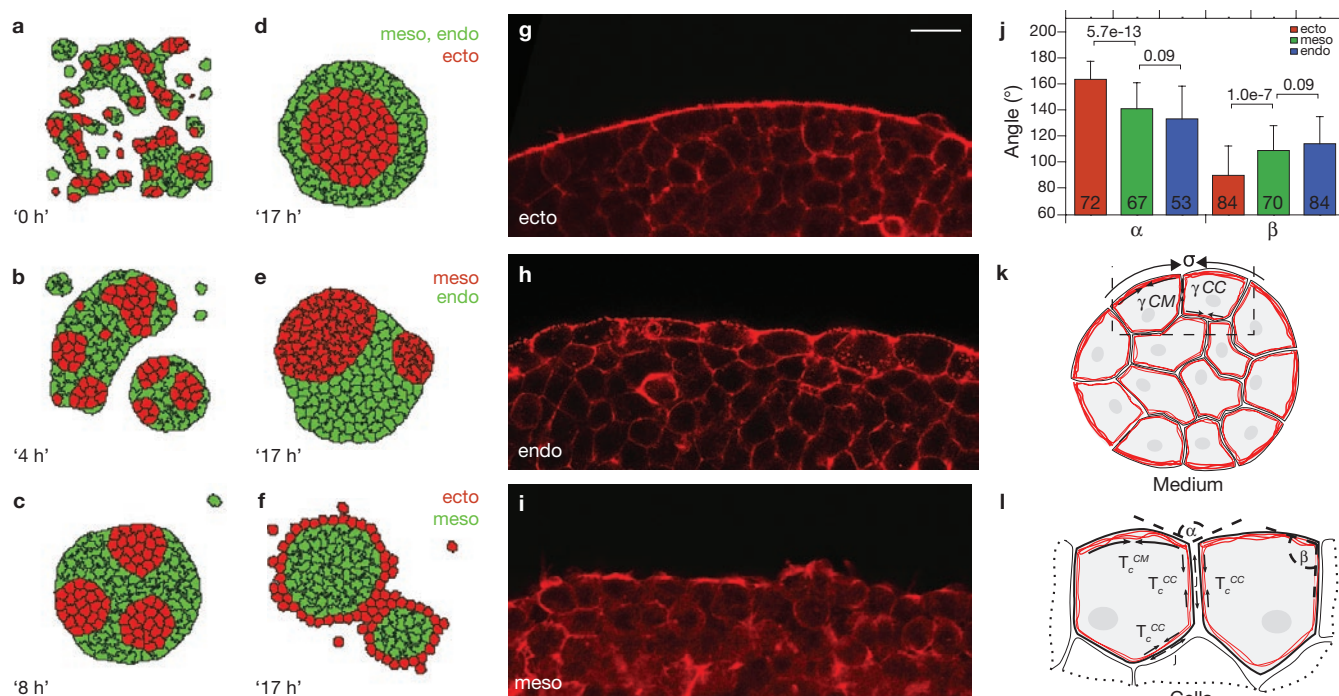


**Figure 4** Simulations of germ-layer progenitor cell sorting using the Cellular Potts-Model and germ-layer explant surface analysis. (a–d) Progenitor cell sorting in an aggregate consisting of ectoderm (red) and mesoderm (or endoderm) cells (green) at consecutive stages of sorting. (e) Stable configuration of mesoderm (red)–endoderm (green) aggregates. (f) Stable configuration of ectoderm (red)–mesoderm (green) aggregates with reduced cell–cortex tension in ectoderm cells. (g–k) Germ-layer explant surface analysis. (g–i) Actin (phalloidin)-staining of ectoderm (g), endoderm (h) and mesoderm (i) explants. Similar results for actin localization were observed using FITC-labelled actin monomers (data not shown). (j) Summary of the two angles  $\alpha$  and  $\beta$  between two cells at the surface of a homotypic aggregate (for angle

representation see l). Data are mean  $\pm$  s. d. Validity of the angle measurement was confirmed with  $0.5\alpha + \beta = 180 \pm$  s. d.; actual  $P$  values are given above the brackets; number of observations are within the bars. (k) Aggregate surface tension (results from the difference between the interfacial tension at the cell-to-cell ( $\gamma^{CC}$ ) and cell-to-medium ( $\gamma^{CM}$ ) interface). (l) The cellular origin of interfacial tension. At the cell-to-medium interface there is no adhesion, thus the interfacial tension  $\gamma^{CM}$  is equal to the cortical tension  $T_c^{CM}$ . The surface tension  $\sigma$  is therefore increased by cell–cortex tension at the cell-to-medium interface and the adhesion between the cells within the aggregate. Scale bar in g, 20  $\mu$ m.

Relative values for adhesion were similar to those measured in Fig. 1c with homotypic adhesion ( $J_{endo} > J_{meso} > J_{ecto}$ ) and heterotypic adhesion ( $J_{ecto,meso} = J_{ecto,endo} = J_{meso,endo}$  = homotypic adhesion  $J_{ecto}$ ). Adhesion of cells to the medium was set to zero.

We simulated progenitor cell sorting using two different conditions: in the first case, cell–cortex tension was assumed to be homogeneous for the whole cell, independent of interactions with other cells or the medium (interface-independent tension). Relative tension values were set according to the experimental data shown in Fig. 2d with  $T_c^{ecto} > T_c^{meso} > T_c^{endo}$ . In the second case, we regarded the tension measurements of Fig. 2d as representative of only the cell-to-medium interface, as proposed previously<sup>11</sup>, with  $T_c^{ecto/medium} > T_c^{meso/medium} > T_c^{endo/medium}$  (interface-specific tension). In contrast, cortex tension at cell-to-cell interfaces was equal for all progenitor types.

When we simulated tissue self-assembly under conditions of interface-independent tension, ectoderm cells enveloped both mesoderm and endoderm progenitors (data not shown), contrary to our experimental observations (Fig. 3b–e). In contrast, under conditions of interface-specific tension, progenitors sorted exactly as observed in the experiments, with mesoderm and endoderm progenitors surrounding ectoderm (Fig. 4a–d) and ectoderm progenitors with reduced cortex tension surrounding mesoderm progenitors (Fig. 4f). This suggests that interfacial energy resulting from adhesion and cell–cortex tension can

trigger germ-layer progenitor sorting if differential cortex tension exists at the cell-to-medium interface.

To determine whether differences in actomyosin-dependent cell–cortex tension exist at the cell-to-medium interface, we stained ectoderm, mesoderm and endoderm tissue explants after 7 h in culture with the F-actin marker phalloidin. All explants showed uniform intensity of cortical actin staining at cell-to-cell interfaces, whereas elevated actin staining was seen at the cell-to-medium interface (the surface of the explants; Fig. 4g–i). In addition, the surface of ectoderm explants was straighter (Fig. 4j) and displayed higher cortical actin levels than mesoderm and endoderm explants (Fig. 4g–i), suggesting higher tension at the cell-to-medium interface of ectoderm explants. Together, these findings support the prediction from our simulations that cortex tension at the cell-to-medium interface is different between ectoderm and mesoderm cells. The findings are also consistent with our previous observations that tissue surface tension is higher in ectoderm versus mesoderm explants<sup>17</sup>.

Questions remain as to the relevance of progenitor sorting *in vitro* for their actual morphogenetic behaviour *in vivo*. To compare progenitor sorting *in vitro* and *in vivo*, we therefore established an *in vivo* cell sorting assay system. We transplanted ectoderm, mesoderm or endoderm progenitors into the blastoderm margin of maternal-zygotic *one-eyed-pinhead* (MZ-*oep*) mutant embryos, which consist predominantly of ectoderm progenitors<sup>16</sup>, and then monitored the sorting behaviour

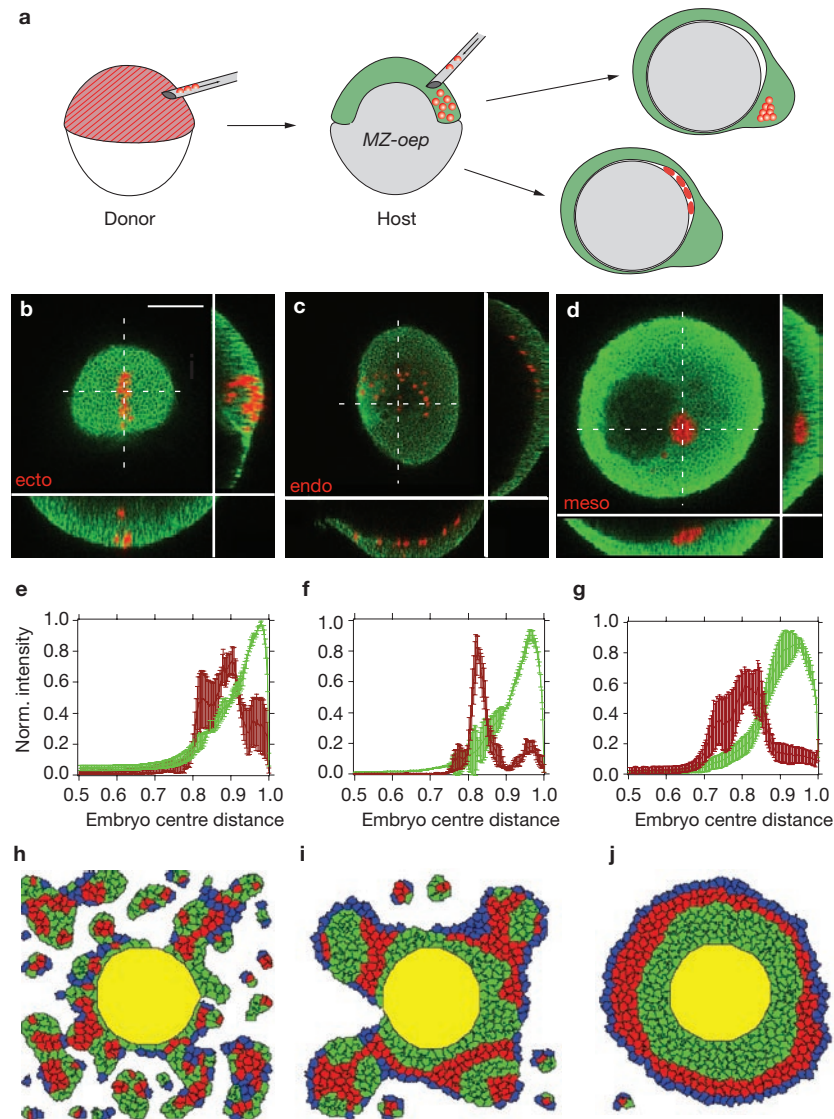


**Figure 5** Sorting of germ-layer progenitor cells *in vivo* (a) Schematic drawing of an *in vivo* progenitor cell sorting assay. Progenitor cells from different embryos (donor, red) were transplanted into an MZ-oepl mutant embryo (host, green) at shield stage (6 hpf) and sorting of donor and host cells was observed at bud stage (10 hpf). Two different possible outcomes are represented schematically: spreading of donor cells between epiblast and yolk or integration of donor cells into the epiblast of the host embryo. (b–d) Localization of donor ectoderm ( $n = 9$  embryos; b), endoderm ( $n = 7$ ; c) and mesoderm ( $n = 7$ ; d) progenitor cells in MZ-oepl mutant embryos at bud stage. Dorsal views. Images were constructed in Leica SP5 LAS software. (e–g) Analysis of the spatial configuration of transplanted donor (red) and host (green) cells depicted as normalized (norm.) intensity as a function of the distance from the centre of the embryo. Ectoderm cells overlapped more strongly with host tissues compared with mesoderm

between the transplanted donor cells and the host cells of the recipient embryo (Fig. 5a). When ectoderm progenitors were transplanted into MZ-oepl embryos at shield stage (6 hpf), they remained as a loosely coherent cluster of donor cells embedded in the epiblast of the host embryo at bud stage (10 hpf; Fig. 5b, e). In contrast, when mesoderm or endoderm progenitors were transplanted into the germ-ring of a shield stage MZ-oepl host embryo, they segregated from the host cells and either arranged into a compact cell cluster (mesoderm; Fig. 5d, g) or dispersed as single cells

and endoderm cells. (h–j) Simulation of consecutive steps of progenitor cell sorting in the presence of extra-embryonic EVL and yolk cell. Adhesion and tension values for mesoderm and ectoderm progenitors were set as in Fig. 4. We further assumed that EVL cells adhere preferentially to ectoderm progenitors ( $J_{evl,ecto} > J_{evl,meso}$ ), that yolk and EVL cells have uniform contraction (not interface-specific) and that the adhesion between yolk and the germ-layer progenitors is equal to the homotypic adhesion of germ-layer progenitors ( $J_{yolk,meso} = J_{meso,meso}$ ,  $J_{yolk,ecto} = J_{ecto,ecto}$ ). This results in mesoderm progenitors adhering more strongly to the yolk than do ectoderm progenitors. Progenitor cell sorting was simulated with one big yolk cell (yellow) mixed with 10% EVL cells (blue), 45% ectoderm (red) and 45% mesoderm (green) progenitors. Similarly to the *in vivo* situation, EVL cells were found at the outside, yolk at the centre and ectoderm cells surrounding mesoderm. Scale bar in b, 150  $\mu\text{m}$ .

(endoderm; Fig. 5c, f) between the yolk cell and the overlying epiblast at bud stage. These experiments suggest that *in vitro* and *in vivo* sorting of germ-layer progenitors retains common and divergent features. In both cases, ectoderm progenitors segregate from mesoderm and endoderm progenitors into distinct cell clusters that contact each other. However, the position of ectoderm relative to mesoderm and endoderm differs; ectoderm is on the inside of heterotypic aggregates *in vitro*, but more superficial to mesoderm and endoderm *in vivo*.

The apparent discrepancy in the final positioning of germ-layer progenitors is probably due to progenitor sorting *in vivo* being influenced by interactions with extra-embryonic tissues such as the enveloping cell layer (EVL) on the outside of the embryo and the yolk cell on the inside (initial source of Nodal signals), which are not present in our *in vitro* preparations. To test this hypothesis, we simulated progenitor cell sorting in the presence of the yolk cell and EVL cells. Assuming both strong adhesion of ectoderm progenitors to the EVL<sup>24</sup> and mesoderm cells to the yolk syncytial layer (YSL)<sup>5</sup>, progenitor sorting was similar to that *in vivo* (Fig. 5h–j; Supplementary Information, Fig. S4), suggesting that our progenitor adhesion and tension measurements can predict the *in vivo* sorting order when additional parameters, such as EVL or yolk-cell adhesion are included. This view is also supported by experiments showing that when the blastoderm margin is removed from the embryo and placed in culture, endogenous mesoderm and ectoderm, in the absence of EVL and yolk, self-assemble into an inside-out configuration, similarly to the *in vitro* sorting experiments<sup>17</sup>.

The Differential Adhesion Hypothesis<sup>26</sup>, one of the most prevalent hypotheses in the field, proposes that cell sorting and tissue organization result from disparate adhesiveness of the participating cells. Here we show that differential intercellular adhesion of germ-layer progenitors alone is not sufficient to explain their sorting behaviour and that differences in actomyosin-dependent cell-cortex tensions are critical. How can differences in cortex tension between progenitor types influence their sorting behaviour? Cells sort according to their aggregate surface tension: the aggregate with the lower surface tension surrounds the one with the higher surface tension. Aggregate surface tension ( $\sigma$ ) characterizes the tendency of the global aggregate surface area to decrease. It is therefore increased by the tension at the interface between cells and the medium ( $\gamma^{\text{CM}}$ , the tendency of each cell to decrease its cell-to-medium contact area) and decreased by the tension at the interface between cells ( $\gamma^{\text{CC}}$ , the tendency of each cell to decrease its cell-to-cell contact area; Fig. 4k; ref. 22). Thus high tension at the cell-to-medium interface in combination with low tension at the cell-to-cell interface causes high aggregate surface tension. Tension at the cell-to-cell interface ( $\gamma^{\text{CC}}$ ), in turn, is the result of cortical tension minus adhesion at this interface, whereas tension at the cell-to-medium interface ( $\gamma^{\text{CM}}$ ) is determined by cortical tension only (Fig. 4l; refs 23, 27). For cell-cortex tension to increase aggregate surface tension and to influence sorting behaviour, it must increase the difference between  $\gamma^{\text{CC}}$  and  $\gamma^{\text{CM}}$ : it must be higher at the cell-to-medium interface than the cell-to-cell interface. Similarly, cell-cell adhesion increases aggregate surface tension by diminishing cell-to-cell tension. It is thus important that both interface-specific cortex tension and differential adhesion should be taken into account to explain progenitor sorting<sup>27</sup>.

Whether differential adhesion and tension are the only factors determining progenitor sorting *in vivo*, or whether other factors such as directed cell migration, epithelialization and extracellular matrix deposition, are also involved, remains to be determined. Notably, none of the forming germ layers in zebrafish show obvious epithelial characteristics or clearly localized extracellular matrix depositions<sup>9</sup>, leaving directed cell migration as the most likely process to function together with adhesion and tension in germ-layer organization. Future experiments analysing the specific migratory behaviour of germ-layer progenitors will be required to reveal the relative contribution of cell migration to germ-layer formation during zebrafish gastrulation. □

## METHODS

**Injections of mRNA and morpholino oligonucleotides.** To generate endoderm or mesoderm progenitors, one-cell-stage wild-type *tub longfin* embryos were injected with *casanova* (*cas*) mRNA (50 pg) or *cyclops* (*cyc*) mRNA (100 pg) and *cas* morpholino oligonucleotides (2 ng; GeneTools), respectively<sup>28,29</sup>. For ectoderm progenitors, *MZ-oeq* were used<sup>16</sup>. The specific identity of germ-layer progenitors was determined by *in situ* staining of the injected embryos (Supplementary Information, Fig. S1a–p). Embryos injected with *cas* mRNA ubiquitously expressed the endoderm marker *Sox17* (ref. 28), suggesting that cells were fated to become endoderm. We confirmed that the results obtained with *cas*-expressing cells were due to their endoderm character rather than being a specific effect of *cas* overexpression by showing similar adhesive and tensile properties in progenitors from embryos ubiquitously expressing dominant active *daTARAM-A* (50 pg), previously shown to induce endoderm cell fate upstream of *cas*<sup>28</sup> (Supplementary Information, Fig. S1q, r). Embryos injected with *cyc* mRNA and *cas* morpholino oligonucleotides ubiquitously expressed *gooseoid*, a marker of anterior axial mesoderm, suggesting that they were fated to become anterior axial mesoderm. In general, these injections allowed efficient induction of different progenitor types with many<sup>28,29</sup>, but not necessarily all features of their endogenous counterparts.

**Adhesion measurements.** Plasma-activated cantilevers (Veeco MLCT, nominal spring constant  $k = 30 \text{ mN m}^{-1}$ ) were incubated with concanavalin A (ConA,  $2.5 \text{ mg ml}^{-1}$ , Sigma) overnight at  $4^\circ\text{C}$  and carefully rinsed in PBS before use. Plasma-activated microscope slides (GoldSeal) were prepared using a two-well coating mask (nAmbition) to obtain an adhesive and non-adhesive substrate. One well was filled with  $50 \mu\text{l}$  heat-inactivated fetal calf serum (Invitrogen), ensuring passivation of the surface (non-adhesive substrate), whereas the other was filled with  $50 \mu\text{l}$  ConA ( $2.5 \text{ mg ml}^{-1}$ ; adhesive substrate). Before the experiment, substrates were gently rinsed with the cell culture medium used to perform the adhesion tests ( $\text{CO}_2$ -independent DMEM/F-12 1:1 buffered in  $15 \text{ mM}$  HEPES and supplemented with penicillin ( $100 \text{ U ml}^{-1}$ ) and streptomycin ( $0.1 \text{ mg ml}^{-1}$ )). Diluted cell suspensions were then seeded onto the substrate. All experiments were carried out at  $25^\circ\text{C}$ . For homotypic adhesion experiments, cells were selected using phase-contrast microscopy. For heterotypic adhesion experiments, one-cell-stage embryos were injected with both mRNA (see above) and either FITC- or TRITC-coupled dextran (Molecular Probes). Cells were identified using fluorescence microscopy. A given 'probe'-cell (Fig. 1a) was selected from the non-adhesive side of the substrate with a ConA-coated cantilever by gently pressing on it with a controlled force of  $1 \text{ nN}$  for typically  $1 \text{ s}$ . The cell was raised from the surface for  $2\text{--}10 \text{ min}$  to firmly attach to the cantilever. The probe-cell was then moved above a 'target'-cell that was firmly attached to the adhesive ConA-coated part of the substrate. Adhesion experiments ('force-distance cycles', see Fig. 1a) were performed using a  $1 \text{ nN}$  contact force,  $10 \mu\text{m s}^{-1}$  approach and retract velocities, and contact times ranging from  $1\text{--}60 \text{ s}$ . Contact time was varied randomly for a given couple to prevent any systematic bias or history effect. Each condition (that is, same probe-target couple at same contact time) was repeated up to three times, with a resting time of  $30 \text{ s}$  between successive contacts. Each probe-cell was used to test several target-cells. No more than 40 curves were taken with any given probe-cell. Cells were observed continuously during and between the force-distance cycles to judge whether they were intact and stably associated with the cantilever/substrate. Only cells that showed characteristic 'ruffling' behaviour and pseudopod formation were used. Target-cell pictures were taken to measure diameter and observe morphology. Force-distance curves were analysed using IgorPro custom-made routines to extract maximum adhesion force (Fig. 1b) and cell deformation (Fig. 1d) during the contact. Data were then pooled and statistically processed as described in Supplementary Information. Cadherin-dependence of cell adhesion was tested after depleting calcium by adding EGTA ( $5 \text{ mM}$ , Sigma) to the medium, or injecting embryos with *E-cadherin* morpholino oligonucleotides ( $8 \text{ ng}$ ; Fig. 1e). To reduce actomyosin function, cells were pre-incubated in (–)-blebbistatin ( $50 \mu\text{M}$ , Sigma). Experiments were carried out in  $5 \mu\text{M}$  (–)-blebbistatin with no more than  $15\text{--}20$  repeated measures taken with a single probe-cell because of mechanical fragility of the treated cells. Preparation of E-cadherin-coated substrates was carried out as described previously<sup>8</sup>. Approach and retract velocities were set to  $4 \mu\text{m s}^{-1}$ .

**Cell-cortex tension measurements and liquid droplet model assumptions.** Colloidal force probes were prepared by attaching a glass bead ( $5 \mu\text{m}$  diameter, Kisker Biotech) to a cantilever (Veeco MLCT) using a two-component Araldit epoxy glue. Such beads were used as an indenter to create a large and smooth contact geometry

with the cell, hence reducing the strain induced by the pressure during contact<sup>60</sup>. To prevent non-specific adhesion to the cells, the modified cantilevers were either incubated with heat inactivated fetal calf serum (Invitrogen) or silanized (1% methyltriethoxysilane (Sigma) in hexane (Fluka) for 1 h) and then passivated with 1% pluronic F127 (Sigma) in ultrapure water. The cells were seeded on a glass substrate. Force-distance curves were acquired using 500 pN contact force and 1  $\mu\text{m s}^{-1}$  approach/retract velocity and indentation;  $\delta$ , was calculated from tip displacement (Fig. 2b). Up to three curves, with at least 15 s waiting time between successive curves, were taken per cell to prevent any history effect<sup>30</sup>. To describe the mechanics of the different cell types by AFM indentation, the approach of Rosenbluth *et al.*<sup>31</sup> was chosen. The liquid droplet model<sup>13</sup> was applied to extract the cell-cortex tension, as previously proposed for different cell lines using the micropipette technique<sup>31,14,32</sup>. Cell-cortex tension is influenced directly by the state of the contractile apparatus of the cell<sup>2,14</sup>. The liquid droplet model describes the cell as a viscous cytosol surrounded by an elastic (actin-based) cortex. This is based on the following assumptions: 1) an actin cortex exists in close proximity to the cell membrane, and the nucleus occupies only a small volume of the cell; 2) cells are not adherent and spherical; 3) force versus indentation curves are linear (see equation below); 4) indentation depth is small, compared with the size of the cell; 5) cell-cortex tension is independent of the cantilever speed; 6) cells have a large plasma-membrane reservoir. Cell-cortex tension  $T_c$  can then be calculated using the following equation<sup>32</sup>:

$$F = \left[ 2T_c \left( \frac{1}{R_c} + \frac{1}{R_b} \right) \times 2\pi R_b \right] \times \delta$$

( $F$  = force,  $\delta$  = indentation,  $R_c$  = cell radius and  $R_b$  = bead radius). Phalloidin staining of our progenitors showed an actin-based cortex both in dissociated cells and in embryos (Fig. 2a). The ratio of cell- to nucleus- volume estimated from phase-contrast images was high ( $21 \pm 12$ , mean  $\pm$  s. d.). Dissociated cells were roughly spherical (Figs. 2a; Supplementary Information, Fig. S2c) and weakly adherent to the substrate. Force versus indentation curves were linear (70% of all curves) for a large range of indentation values (Fig. 2b), with the deformation (max  $\sim 1 \mu\text{m}$ ) being at least one order of magnitude smaller than the cell diameter (approximately 18–20  $\mu\text{m}$ ). Furthermore, we did not find a strong influence of the cantilever speed on cell-cortex tension (data not shown). Finally, our adhesion measurements suggest that the cells possess a large membrane reservoir as indicated by long lipid tubes extracted during the separation process using SCFS (tethers, Fig. 1a). Together, this provides experimental support for using the liquid drop model to analyse our indentation experiments and gain information about the cortex tension of the progenitor types. To determine cell-cortex tension using the equation above, we used a force versus indentation line-fit between 125 pN and 250 pN to exclude errors that could be introduced while determining the bead-to-cell contact point<sup>33</sup>. Bead and cell radii were determined by phase-contrast microscopy. To alter cortex tension, cells were pre-incubated in (–)-blebbistatin (50  $\mu\text{M}$ ) or recombinant activin (100 ng ml<sup>-1</sup>, Sigma) for 2 h. For blebbistatin, cells were measured in the presence of 5  $\mu\text{M}$  (–)-blebbistatin. All experiments were performed at 25°C.

Note: Supplementary Information is available on the Nature Cell Biology website.

#### ACKNOWLEDGEMENTS

We thank Pierre Bongrand, Wayne Brodland, Jonne Helenius, Mathias Köppen, Andy Oates, Ewa Paluch, Laurel Rohde, Erik Schäffer, Clemens Franz, Sylvia Schneider, Petra Stockinger, Anna Taubenberger, Florian Ulrich and Simon Wilkins for fruitful discussions; Stan Marée for sharing the simulation code for the Cellular-Potts-Model; Lara Carvalho for sharing unpublished results; JPK Instruments for technical support; Jonne Helenius for supporting data analysis procedures and the fifth floor seminar club for vibrant discussions. This work was supported by grants from the Boehringer Ingelheim Fonds to M. K., Deutsch-Französische Hochschule to M. K. and P. H. P. and the Deutsche Forschungsgemeinschaft to C. P. H.

#### AUTHOR CONTRIBUTIONS

M. K. performed and analysed the AFM and biochemical experiments and the hanging drop cell aggregation/sorting experiments; Y. A. performed the molecular biology experiments, embryo injections, cell culture work (sorting and explant analysis), cell transplantations and *in situ* hybridizations; J. K. performed the simulation experiments and contributed to image analysis; C. P. H., D. M., F. G. and P. H. P. conceived and designed the experiments; M. K., C. P. H., D. M. and P. H. P. prepared the manuscript.

Published online at <http://www.nature.com/naturecellbiology/>

Reprints and permissions information is available online at <http://npg.nature.com/reprintsandpermissions/>

1. Tepass, U., Godt, D. & Winklbauer, R. Cell sorting in animal development: Signalling and adhesive mechanisms in the formation of tissue boundaries. *Curr. Opin. Genet. Dev.* **12**, 572–582 (2002).
2. Montero, J. A. & Heisenberg, C. P. Gastrulation dynamics: Cells move into focus. *Trends Cell Biol.* **14**, 620–627 (2004).
3. Brodland, G. W. The differential interfacial tension hypothesis (dith): a comprehensive theory for the self-rearrangement of embryonic cells and tissues. *J. Biomech. Eng.* **124**, 188–197 (2002).
4. Benoit, M., Gabriel, D., Gerisch, G. & Gaub, H. E. Discrete interactions in cell adhesion measured by single-molecule force spectroscopy. *Nature Cell Biol.* **2**, 313–317 (2000).
5. Puech, P. H., Poole, K., Knebel, D. & Muller, D. J. A new technical approach to quantify cell-cell adhesion forces by afm. *Ultramicroscopy* **106**, 637–644 (2006).
6. Zhang, X. *et al.* Atomic force microscopy measurement of leukocyte-endothelial interaction. *Am. J. Physiol. Heart Circ. Physiol.* **286**, H359–367 (2004).
7. Gumbiner, B. M. Regulation of cadherin-mediated adhesion in morphogenesis. *Nature Rev. Mol. Cell Biol.* **6**, 622–634 (2005).
8. Ulrich, F. *et al.* Wnt11 functions in gastrulation by controlling cell cohesion through Rab5c and E-cadherin. *Dev. Cell* **9**, 555–564 (2005).
9. Montero, J. A. *et al.* Shield formation at the onset of zebrafish gastrulation. *Development* **132**, 1187–1198 (2005).
10. Geiger, B. *et al.* Broad spectrum pan-cadherin antibodies, reactive with the C-terminal 24 amino acid residues of N-cadherin. *J. Cell Sci.* **97**, 607–614. (1990).
11. Harris, A. K. Is cell sorting caused by differences in the work of intercellular adhesion? A critique of the steinberg hypothesis. *J. Theor. Biol.* **61**, 267–285 (1976).
12. Dai, J., Ting-Beall, H. P., Hochmuth, R. M., Sheetz, M. P. & Titus, M. A. Myosin I contributes to the generation of resting cortical tension. *Biophys. J.* **77**, 1168–1176 (1999).
13. Evans, E. & Yeung, A. Apparent viscosity and cortical tension of blood granulocytes determined by micropipet aspiration. *Biophys. J.* **56**, 151–160 (1989).
14. Thoumine, O., Cardoso, O. & Meister, J. J. Changes in the mechanical properties of fibroblasts during spreading: A micromanipulation study. *Eur. Biophys. J.* **28**, 222–234 (1999).
15. Schier, A. F. Nodal signaling in vertebrate development. *Annu. Rev. Cell Dev. Biol.* **19**, 589–621. (2003).
16. Gritsman, K. *et al.* The EGF-CFC protein one-eyed pinhead is essential for nodal signaling. *Cell* **97**, 121–132 (1999).
17. Schötz, E.-M. *et al.* Quantitative differences in tissue surface tension influence zebrafish germ layer positioning. *HFSP J.* **2**, 42–56 (2008).
18. Davis, G. S., Phillips, H. M. & Steinberg, M. S. Germ-layer surface tensions and “tissue affinities” in *Rana pipiens* gastrulae: quantitative measurements. *Dev. Biol.* **192**, 630–644 (1997).
19. Marlow, F., Topczewski, J., Sepich, D. & Solnica-Krezel, L. Zebrafish Rho kinase 2 acts downstream of Wnt11 to mediate cell polarity and effective convergence and extension movements. *Curr. Biol.* **12**, 876–884 (2002).
20. Maree, A. F. M., Grieneisen, V. A. & Hogeweg, P. The Cellular Potts Model and biophysical properties of cells, tissues and morphogenesis. in *Single Cell-Based Models in Biology and Medicine* (eds Anderson, A. R. A., Chaplain, M. & Rejniak, K. A.) 107–136 (Birkhäuser Verlag, Basel; 2007).
21. Ouchi, N. B., Glazier, J. A., Rieu, J.-P., Upadhyaya, A. & Sawada, Y. Improving the realism of the cellular potts model in simulations of biological cells. *Physica A: Stat. Mech. Applic.* **329**, 451–458 (2003).
22. Graner, F. Can surface adhesion drive cell-rearrangement? Part I: Biological cell-sorting. *J. Theoret. Biol.* **164**, 455–476 (1993).
23. Kafer, J., Hayashi, T., Maree, A. F. M., Carthew, R. W. & Graner, F. Cell adhesion and cortex contractility determine cell patterning in the *Drosophila* retina. *Proc. Natl Acad. Sci. USA* **104**, 18549–18554 (2007).
24. Shimizu, T. *et al.* E-cadherin is required for gastrulation cell movements in zebrafish. *Mech. Dev.* **122**, 747–763 (2005).
25. Waga, R. M. & Kane, D. A. A role for N-cadherin in mesodermal morphogenesis during gastrulation. *Dev. Biol.* **310**, 211–225 (2007).
26. Steinberg, M. S. Differential adhesion in morphogenesis: A modern view. *Curr. Opin. Genet. Dev.* **17**, 281–286 (2007).
27. Lecuit, T. & Lenne, P. F. Cell surface mechanics and the control of cell shape, tissue patterns and morphogenesis. *Nature Rev. Mol. Cell Biol.* **8**, 633–644 (2007).
28. Aoki, T. O. *et al.* Molecular integration of casanova in the nodal signalling pathway controlling endoderm formation. *Development* **129**, 275–286 (2002).
29. Carmany-Rampey, A. & Schier, A. F. Single-cell internalization during zebrafish gastrulation. *Curr. Biol.* **11**, 1261–1265 (2001).
30. Dimitriadis, E. K., Horkay, F., Maresca, J., Kachar, B. & Chadwick, R. S. Determination of elastic moduli of thin layers of soft material using the atomic force microscope. *Biophys. J.* **82**, 2798–2810 (2002).
31. Rosenbluth, M. J., Lam, W. A. & Fletcher, D. A. Force microscopy of nonadherent cells: A comparison of leukemia cell deformability. *Biophys. J.* **90**, 2994–3003 (2006).
32. Lomakina, E. B., Spillmann, C. M., King, M. R. & Waugh, R. E. Rheological analysis and measurement of neutrophil indentation. *Biophys. J.* **87**, 4246–4258 (2004).
33. Crick, S. L. & Yin, F. C. Assessing micromechanical properties of cells with atomic force microscopy: Importance of the contact point. *Biomech. Model. Mechanobiol.* **6**, 199–210 (2007).

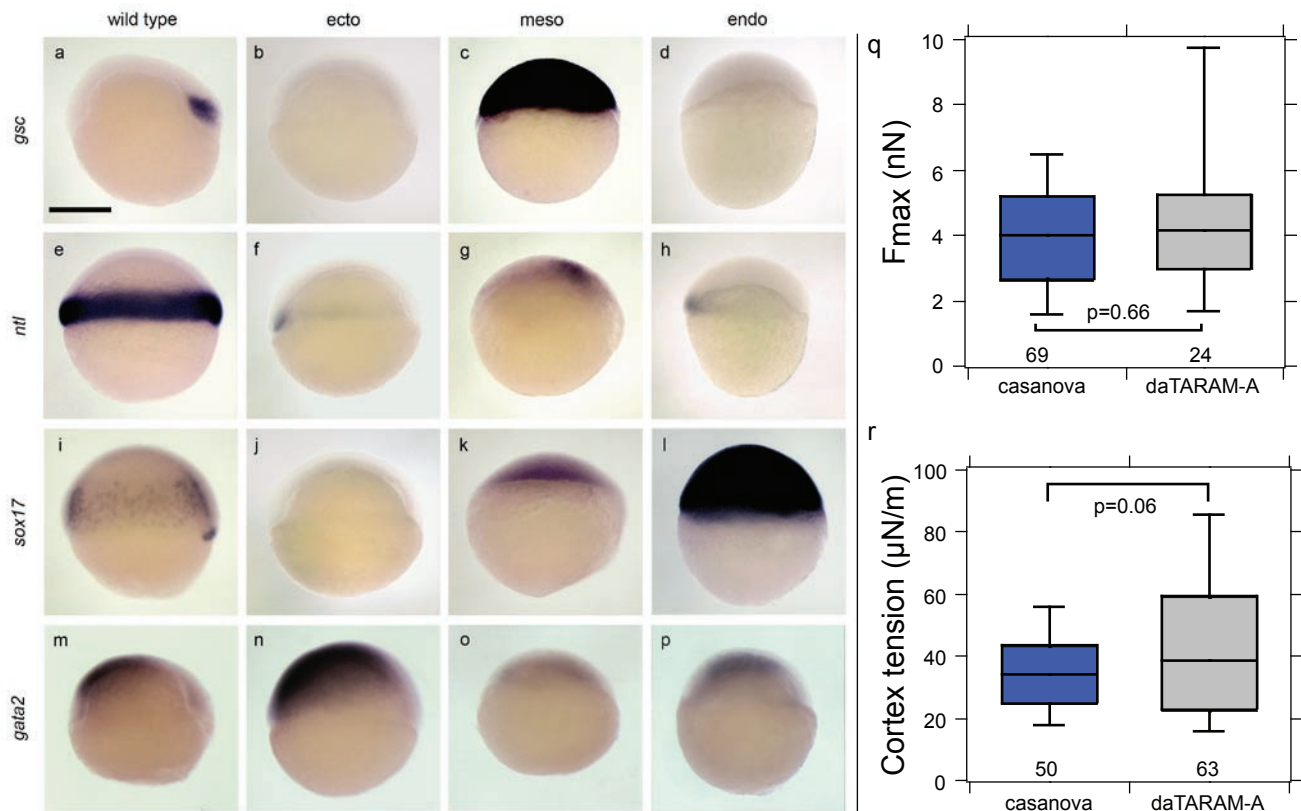


**Figure S1** Germ layer progenitor cell identities. Whole mount *in situ* hybridization for *gsc* (anterior axial mesoderm-prechordal plate; **a-d**), *ntl* (mesoderm; **e-h**), *sox17* (endoderm; **i-l**) and *gata2* (ventral ectoderm; **m-p**) expression in wild type (**a,e,i,m**), *MZ-oepl* (ecto; **b,f,j,n**), *cyc mRNA+cas MO* (meso; **c,g,k,o**), and *cas mRNA* (endo; **d,h,l,p**) injected embryos. Scale bar in

(**a**)=250  $\mu\text{m}$ . (**q,r**) Endoderm progenitor cell adhesion and tension induced by dominant active *TARAM-A*.  $F_{max}$  for homotypic adhesion (**q**) and cortex tension (**r**) of endoderm cells obtained by expressing either *cas mRNA* (50 pg/embryo) or dominant active *TARAM-A mRNA* (*daTARAM-A*; 50 pg/embryo). Actual *p*-values are given above/below the brackets, number of observations below the whiskers.

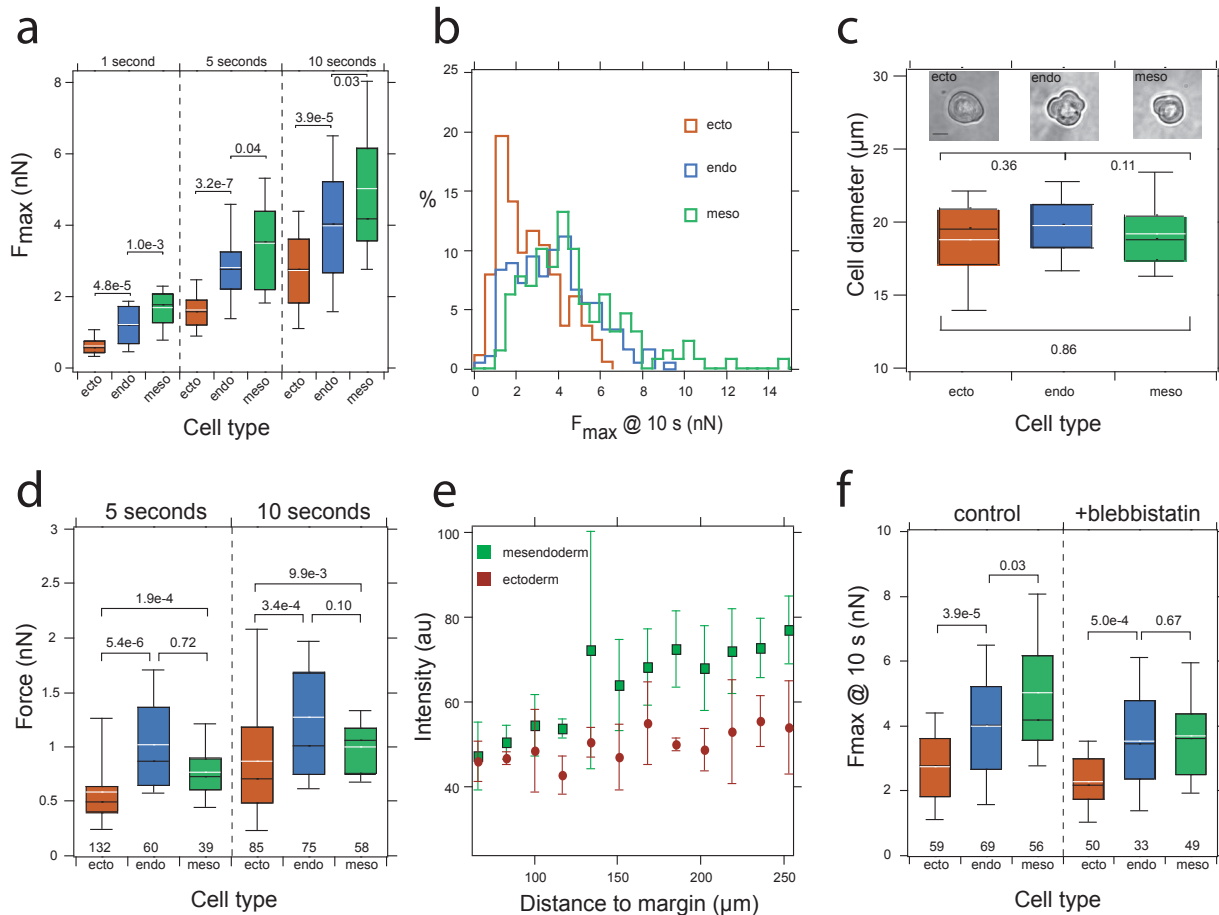


**Figure S2** Germ layer progenitor cell adhesion and cell size **(a)**  $F_{max}$  of homotypic progenitor cell adhesion as a function of contact time displayed as box-whisker plots. Median in black and mean in white. Numbers above/below brackets indicate  $p$  values for the corresponding combinations. **(b)** Distribution of  $F_{max}$  for the three progenitor cell types at 10 s contact time. Unprocessed raw data; binning set to 500 pN. **(c)** Box-whisker plot of the cell diameter for different progenitor cell types. Numbers above/below brackets indicate  $p$  values for the corresponding combinations. Phase contrast micrographs of typical progenitor cell morphology used in the SCFC experiments are shown above the box-whisker plots. Scale bar: 10  $\mu\text{m}$ . **(d-f)**

Involvement of Cadherin and Myosin in progenitor cell adhesion. **(d)**  $F_{max}$  as a function of contact time for progenitor cell adhesion to an E-cadherin-coated surface. **(e)** Intensity profile of E-cadherin staining in the hypoblast (mesoderm and endoderm progenitors) and epiblast (ectoderm progenitors) determined from Fig. 1f. E-cadherin plasma membrane intensities are higher in cells of the anterior axial hypoblast compared to adjacent epiblast cells. **(f)** Quantification of  $F_{max}$  for homotypic adhesion as a function of germ layer progenitor cell type in the presence or absence of Blebbistatin at 10 s contact time. Actual  $p$ -values are given above the brackets, number of observations below the whiskers.

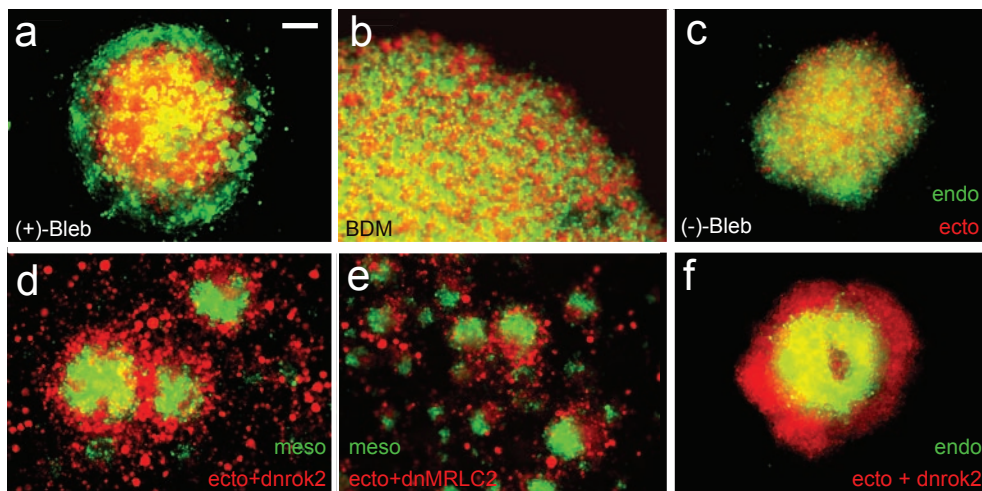


**Figure S3** Germ layer progenitor cell sorting and cortex tension. (a,b) Sorting in mesoderm (green) and ectoderm (red) hanging drop co-cultures in the presence of 50  $\mu$ M (+)-Blebbistatin (a) and 20mM BDM (b) after 17 h in culture. (c) Sorting of ectoderm (red) and endoderm (green) in hanging drop co-cultures in the presence of (-)-Blebbistatin after 17 h in culture. (d-f)

Sorting in mesoderm-ectoderm (d,e) and endoderm-ectoderm (f) hanging drop co-cultures with ectoderm cells (red) expressing either *dnrok2* mRNA (d,f; 350 pg/embryo) or *dnmrlc2a* mRNA (e; 250 pg/embryo) to reduce cortex tension after 17 h in culture. Scale bar in (a)=150  $\mu$ m. Images were constructed in ImageJ.

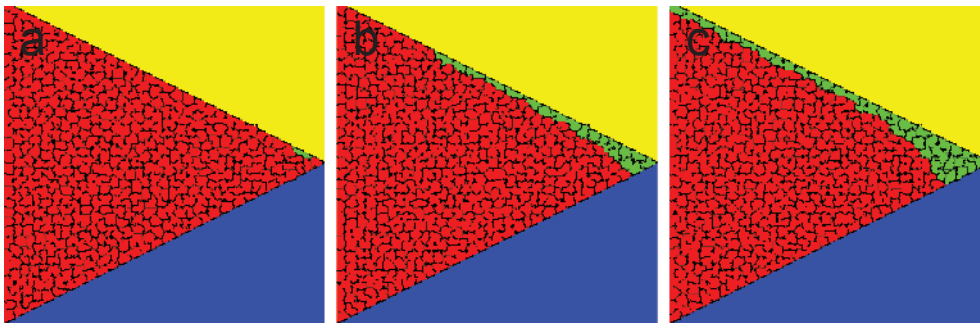


**Figure S4** Simulation of germ layer progenitor cell sorting in the presence of extra-embryonic EVL and yolk cell. Adhesion and tension values for mesoderm and ectoderm progenitors were set as in Fig.4. We further assumed that EVL cells adhere preferentially to ectoderm progenitors ( $J_{evl,ecto} > J_{evl,meso}$ ), that yolk and EVL cells do have uniform contraction (not interface-specific) and that the adhesion between yolk and the germ layer progenitors is equal to the homotypic adhesion of germ layer

progenitors ( $J_{yolk,meso} = J_{meso,meso}$ ,  $J_{yolk,ecto} = J_{ecto,ecto}$ ). **(a-c)** Simulation of consecutive steps of progenitor cell sorting at the germ ring margin with the yolk (yellow) and EVL (blue) positions fixed, the space between yolk and EVL filled with ectoderm cells (red), and the rightmost ectoderm cell differentiating into a mesoderm cell (green) at regular intervals. Similar to the situation at the germ ring margin, mesoderm progenitors disperse between the ectoderm and yolk.

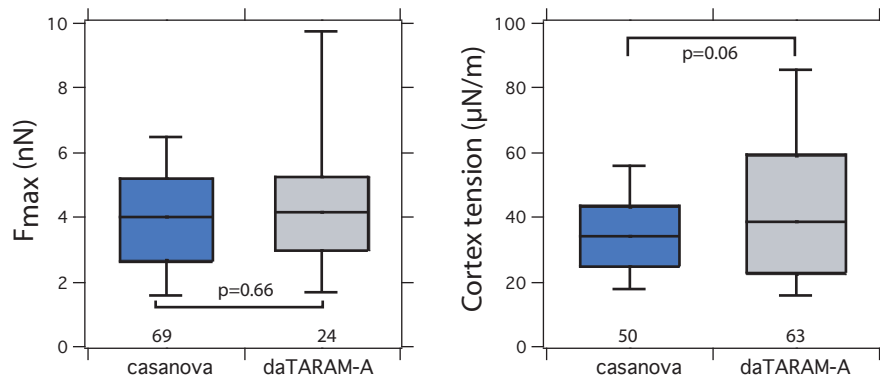


**Figure S5** Endoderm progenitor cell adhesion and tension.  $F_{max}$  for homotypic adhesion (a) and cortex tension (b) of endoderm cells obtained by expressing either *cas* mRNA (50 pg/embryo) or dominant

active *TARAM-A* mRNA (*daTARAM-A*; 50 pg/embryo). Actual *p*-values are given above/below the brackets, number of observations below the whiskers.

## Supplementary Methods

### *Embryo maintenance*

Fish maintenance and embryo collection was carried out as previously described<sup>1</sup>.

### *Primary cell culture*

For cell culture, dome-stage embryos (5 hpf) were dechorionated in 2 mg/mL Pronase (Roche) and transferred into dissociation medium (DMEM/F-12 + 0.5 mg/mL EDTA). The blastoderm was dissociated by gentle mixing to obtain single cells. Yolk remnants were removed by sedimentation in cell culture medium. The dissociation medium was replaced after centrifugation with CO<sub>2</sub>-independent DMEM/F-12+Pen/Strep for SCFS and cortex tension measurements, or DMEM+Pen/Strep for hanging drops and tissue explants.

### *Single-cell force spectroscopy (SCFS) set-up*

Cell-cell adhesion and cell cortex tension measurements were conducted with an AFM (Nanowizard I<sup>®</sup>, JPK Instruments) mounted on an inverted fluorescence microscope (Zeiss Axiovert 200, equipped with 20x and 40x lenses). Either phase-contrast or fluorescence imaging were used to select cells and monitor their morphology during force measurements (see below). The setup was extended with a JPK CellHesion<sup>®</sup> module to increase the cell-cell separation distance up to 100  $\mu$ m and used in closed height feedback mode<sup>2</sup>. Cantilevers were calibrated *in-situ* using the thermal noise method<sup>3</sup> prior to experiments. The calibration procedure for each cantilever was repeated three times to rule out possible errors. Spring constants were found to be consistent with the manufacturer's nominal value (Veeco Instruments).

### *Statistical analysis*

After determining  $F_{max}$  for each force-distance curve, we averaged  $F_{max}$  over the experimental repetitions (see above) to determine the mean adhesion force of a given cell couple and contact time. The resulting values were then pooled to obtain the distribution of adhesion forces for a given experimental condition. The median $\pm$ MAD (median

absolute deviation,  $MAD = median(x_i - \tilde{x})$  and percentiles were then extracted with a custom IgorPro (WaveMetrics) function and used in KaleidaGraph (SynergySoftware) for unpaired Wilcoxon based Mann-Whitney U-tests for significance with a  $p$  cut-off value of 0.05. Exact  $p$  values are given within the figures and were calculated using ' $R$ '. Non-parametric tests were used on all data, because we assumed that the data are not normally distributed. Although no systematic history effect on successive force-distance curves taken with one cell was detected (data not shown), we could not assume that each curve is strictly independent of each other. Furthermore, adhesion force data are likely to be dependent on different properties, e.g. more than one type of adhesion molecule, which does not allow us to use parametric tests. Wilcoxon based Mann-Whitney U-tests are distribution independent and can therefore be applied on composite data-sets. Box-whisker plots are presented with the box containing 50 % of the data around the median and whiskers encompassing 80 % of the data values. Pearson's rank correlation coefficient  $R$  was computed using IgorPro. Values of  $T_c$  for each test were pooled and tested using the same procedure.

#### *Cell aggregation experiment*

Hanging drop experiments were performed as described<sup>5</sup>. In short, embryos at the one-cell-stage were injected with a mix of fluorescently labeled dextran and *mRNAs* to induce homogenic cell fate in the embryo. After blastoderm dissociation at dome-stage (5 hpf),  $1.5 \cdot 10^6$  cells/mL of two different germ layer progenitor cell types were allowed to aggregate in 25  $\mu$ L or 50  $\mu$ L hanging drops. The ratio of co-cultured cells was set to 1:1 or 1:2 with the enveloping cell type at the higher concentration. Cultures were incubated for at least 17 h in a humidified chamber equilibrated with 5 %  $CO_2$  at 27°C. To reduce cortex tension, the cells were cultured in the presence of 50  $\mu$ M (-)-Blebbistatin (CalBioChem), 10 mM Cytochalasin D (Sigma) or 20 mM 2,3-butanedionemoxime (BDM, CalBioChem). Control aggregates were cultured in the presence of 50  $\mu$ M (+)-Blebbistatin (CalBioChem, Fig.S3a). Incubation in 5 mM EDTA did not lead to sorting (data not shown). To selectively inhibit cortex tension in ectoderm progenitors, *MZ-oepr* embryos were injected with 350 pg *dnrok2* *mRNA*. Images were taken after 0, 4, 6, 8 and 17 h in culture with Metamorph (Digital Imaging) using an epifluorescence microscope

(Zeiss Axiovert 200M equipped with EXFO X-cite 120, 5x lens, 470[40]BP/525[50]BP and 546[12]BP/575LP excitation/emission filters) and a CoolSnap CCD camera (Roper Scientific, 4.6x4.6  $\mu\text{m}^2$ , 12 bit pixel). Linear contrast adjustment was applied to the whole image using ImageJ. To analyze the sorting dynamics, 5000 cells of each type were cultured in a passivated micro-chamber. Sorting was followed with a rate of 4 frames/min and analyzed as described below. Culture in EDTA did not lead to any changes in cluster size (Fig.3h).

### *Image analysis*

To extract information about dynamic changes in boundary length or projected particle area during cell sorting, standard plug-ins for ImageJ were used. Images were first ‘binarized’ and ‘despeckled’ to remove single pixels in each frame, followed by ‘erode’ and ‘dilate’ steps. The number of particles was then counted, the area measured and normalized to the number of particles. Western blots were quantified using ImageJ. The average intensity of each single band was measured using equal sized boxes, background was subtracted and then normalized to the intensity of intracellular  $\alpha$ -tubulin. Confocal images of the transplanted embryos were analyzed using ImageJ. The perimeter of the embryo was fitted to a circle and the integrated radial intensity profile was calculated (intensity as a function of the center distance). The corresponding intensity values and distances were normalized and the mean intensity at a given position was calculated. Embryonic shield sections stained for E-cadherin were quantified using ImageJ. Cell boundaries were traced and staining intensity plotted against the distance to the shield.

### *Whole-mount antibody staining and cell surface biotinylation*

Whole-mount E-cadherin antibody staining on sections of gastrula stage embryos were performed as previously described<sup>1</sup>. For surface biotinylation experiments, dome-stage embryos (5 hpf) were dissociated in 1/2 Ringer solution w/o  $\text{Ca}^{2+}$  and washed three times in 1/2 Ringer.  $5 \times 10^6$  cells were incubated at 4°C in 1 mg/mL Sulfo-NHS-biotin in PBS (Pierce Biotechnology, Cell surface biotinylation kit). After 30 min the reaction was quenched and the cells were washed twice in TBS. To separate biotinylated proteins from the intracellular pool, the manufacturer’s protocol was followed. Total protein content

was estimated using a BCA test (Pierce Biotechnology). For Western blotting, equal amounts of mesoderm, endoderm and ectoderm membrane fraction were transferred onto a 10 % polyacrylamide gel. Classical cadherins were detected using a rabbit anti-pan-cadherin antibody (1:5000<sup>6</sup>) and a HRP-coupled secondary donkey anti-rabbit (1:2000, Amersham Bioscience). As loading controls a mouse  $\alpha$ -tubulin antibody (Sigma, 1:2000) was used. Secondary antibody detection was done using a chemiluminescent substrate kit (1:1 ECL kit, Amersham Bioscience) and detected in a FujiFilm LAS 3000 imagereader.

#### *In situ hybridizations*

Whole mount *in-situ* hybridization were performed as described previously<sup>1</sup>. For *gsc*-, *ntl*-, *gata2*- and *sox17*- *in-situs*, antisense RNA probes were synthesized from partial sequences of the respective cDNAs. Pictures were taken with a dissecting scope (Olympus SZX 12) equipped with QImaging Micropublisher 5.0 camera.

#### *Cell transplantations*

Cell transplantations were carried out as described<sup>1</sup>. In short, cells from donors fluorescently labeled with FITC- or TRITC- dextran (Molecular Probes) were transplanted into *MZ-oep:ras-GFP* transgenic hosts at shield stage (6 hpf) and fixed in 4 % paraformaldehyde at bud stage (10 hpf). Optical 3D sections were acquired with an upright Leica SP5 confocal microscope equipped with a 20x water immersion lens using 488 Argon and 633 HeNe laser lines.

#### *Germ layer explants*

Tissue explants followed by Phalloidin staining were carried out as previously described<sup>5</sup>. Pictures were taken with an Zeiss LSM Meta upright microscope using and 543 HeNe laser 542(12)BP excitation and 573LP emission filters.

#### *Numerical simulations*

The *Cellular-Potts-Model*<sup>7</sup> was used to perform simulations on a 2D square lattice, measuring 230x230 pixels. The algorithm for energy minimization is based on Monte Carlo sampling and the Metropolis algorithm (for a detailed description of the procedure

see <sup>7</sup>). An energy is assigned to each cell and interface, with the total energy of a cell aggregate as defined by<sup>8,9</sup>:

$$H = \sum_{\text{interfaces}} P_{ij}(C_{ij} + C_{ji} - J_{ij}) + \sum_{\text{cells}} \lambda_p (P_i - P_0)^2 + \sum_{\text{cells}} \lambda_A (A_i - A_0)^2$$

In this model the adhesion between the cell  $i$  and  $j$  is  $J_{ij}$  and the cortical tension of cell  $i$  at the interface with cell  $j$  is  $T_{ij} = C_{ij} + 2\lambda_p(P_i - P_0)$ . The interfacial tension between cell  $i$  and cell  $j$  is thus  $\gamma_{ij} = T_{ij} + T_{ji} - J_{ij}$ . Differential interfacial tension is modeled by assigning interface-specific values to  $C_{ij}$ .  $\lambda_p$  and  $\lambda_A$  are the perimeter and area moduli,  $P_0$  and  $A_0$  the target perimeter length and area of cell  $i$ . For the adhesion energies we chose  $J_{ecto,ecto}=200$ ,  $J_{endo,endo}=300$ ,  $J_{meso,meso}=400$ ,  $J_{ecto,endo}=J_{ecto,meso}=J_{meso,endo}=200$ , and  $J_{ecto,medium}=J_{meso,medium}=J_{endo,medium}=0$ . To qualitatively represent the differences in the cortical tensions of the cells, we used the following for the simulations in Fig. 4a-e:  $C_{ecto,medium}=300$  and  $C_{meso,medium}=50$  and for all other interfaces,  $C_{ij}=0$ . Other parameter values are  $\lambda_p=0.3$  and  $P_0 = \frac{(\sqrt{\pi A_0})}{10}$ ,  $\lambda_A=25$  and  $A_0=50$  for all cells with a fluctuation allowance  $T=300$ .

### Supplementary References:

1. Montero, J.A. *et al.* Shield formation at the onset of zebrafish gastrulation. *Development* 132, 1187-1198 (2005).
2. Puech, P.H., Poole, K., Knebel, D. & Muller, D.J. A new technical approach to quantify cell-cell adhesion forces by afm. *Ultramicroscopy* 106, 637-644 (2006).
3. Hutter, J.L. & Bechhoefer, J. Calibration of atomic force microscope tips. *Review Scientific Instruments* 64, 1868-1873 (1993).
4. R Development Core Team (R Foundation for Statistical Computing. Vienna, Austria, 2007).
5. Schötz, E.-M. *et al.* Quantitative differences in tissue surface tension influence zebrafish germ layer positioning *HFSP Journal* (in press).
6. Geiger, B. *et al.* Broad spectrum pan-cadherin antibodies, reactive with the c-terminal 24 amino acid residues of n-cadherin. *J Cell Sci* 97, 607-614. (1990).
7. Maresca, A.F.M., Grieneisen, V.A. & Hogeweg, P. The cellular potts model and biophysical properties of cells, tissues and morphogenesis. (Birkhäuser Verlag, Basel; 2007).
8. Ouchi, N.B., Glazier, J.A., Rieu, J.-P., Upadhyaya, A. & Sawada, Y. Improving the realism of the cellular potts model in simulations of biological cells. *Physica A: Statistical Mechanics and its Applications* 329, 451-458 (2003).

9. Kafer, J., Hayashi, T., Maree, A.F.M., Carthew, R.W. & Graner, F. Cell adhesion and cortex contractility determine cell patterning in the drosophila retina. *Proceedings of the National Academy of Sciences* 104, 18549-18554 (2007).

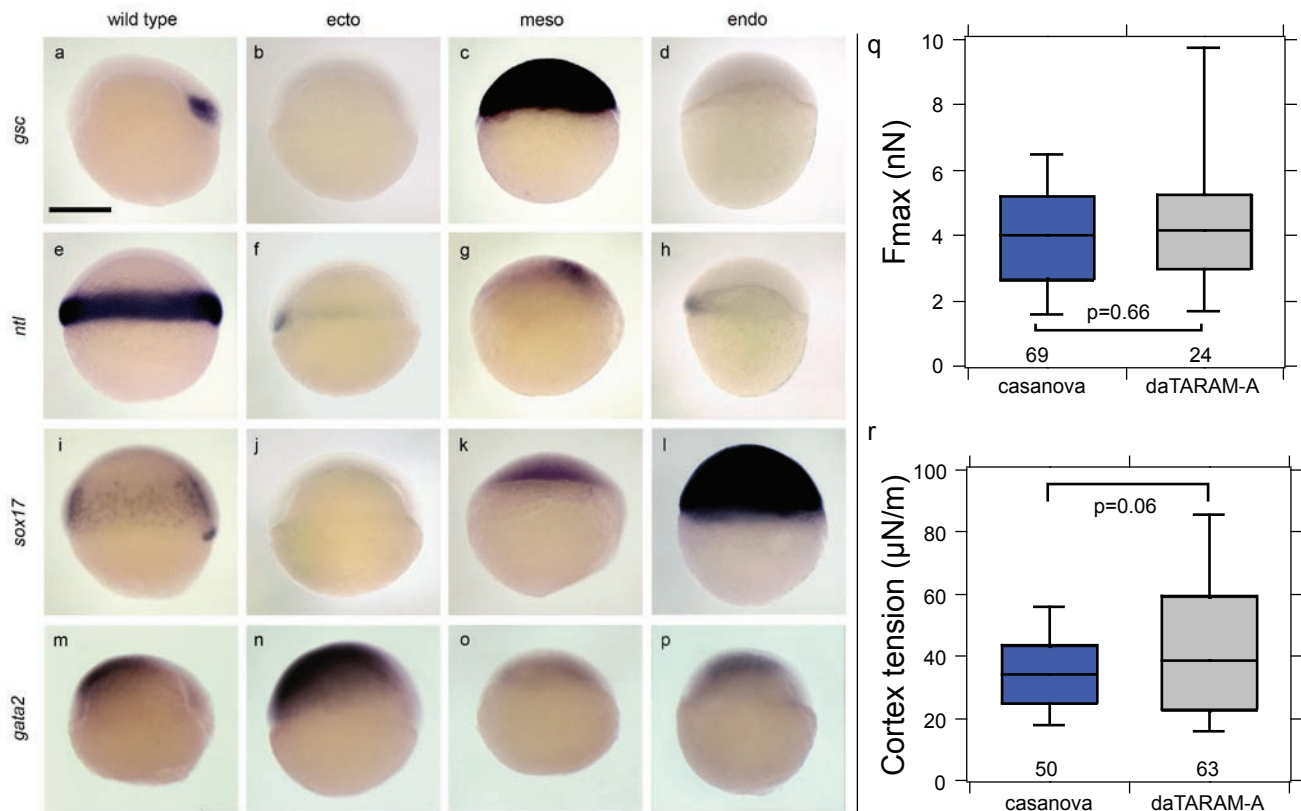


**Figure S1** Germ layer progenitor cell identities. Whole mount *in situ* hybridization for *gsc* (anterior axial mesoderm-prechordal plate; **a-d**), *ntl* (mesoderm; **e-h**), *sox17* (endoderm; **i-l**) and *gata2* (ventral ectoderm; **m-p**) expression in wild type (**a,e,i,m**), *MZ-oepl* (ecto; **b,f,j,n**), *cyc mRNA+cas MO* (meso; **c,g,k,o**), and *cas mRNA* (endo; **d,h,l,p**) injected embryos. Scale bar in

(**a**)=250  $\mu\text{m}$ . (**q,r**) Endoderm progenitor cell adhesion and tension induced by dominant active *TARAM-A*.  $F_{max}$  for homotypic adhesion (**q**) and cortex tension (**r**) of endoderm cells obtained by expressing either *cas mRNA* (50 pg/embryo) or dominant active *TARAM-A mRNA* (*daTARAM-A*; 50 pg/embryo). Actual *p*-values are given above/below the brackets, number of observations below the whiskers.

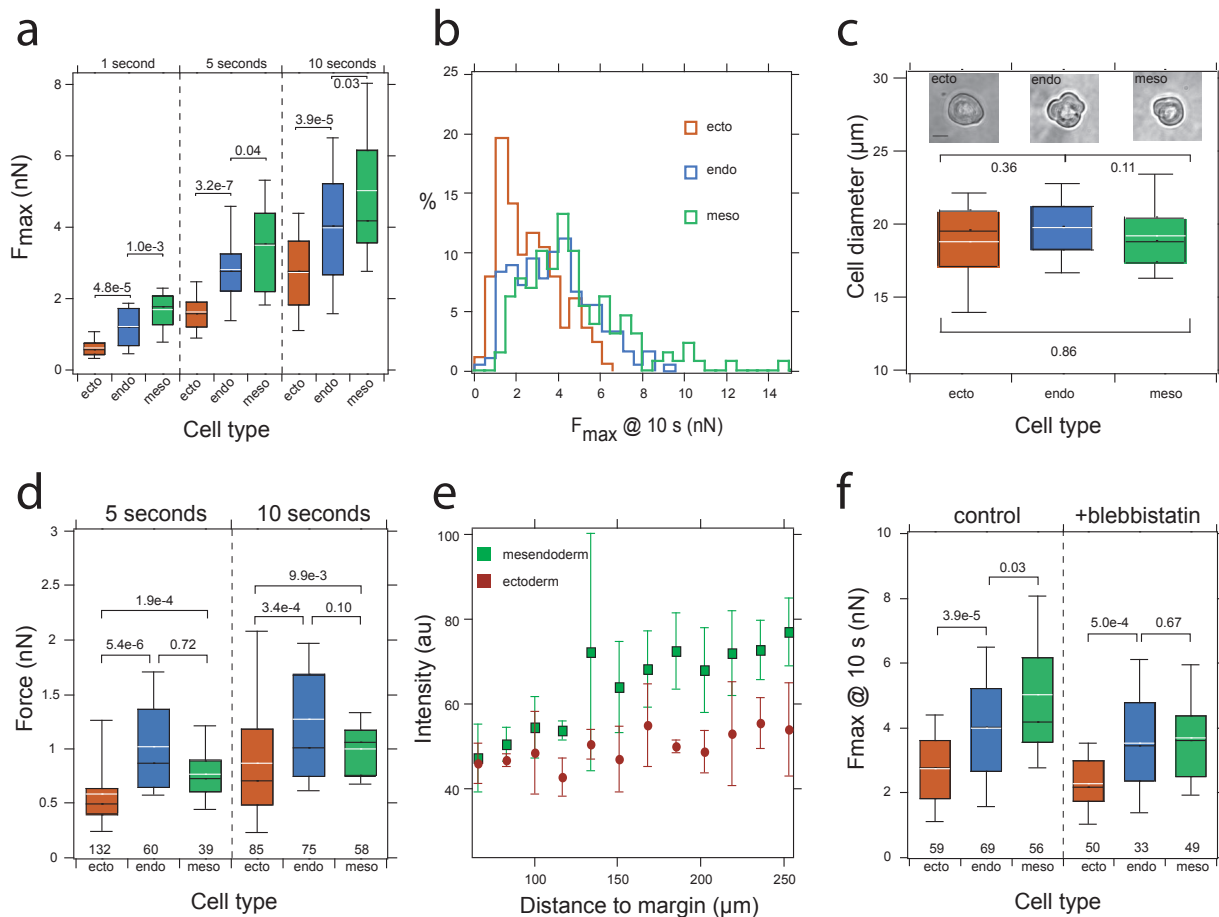


**Figure S2** Germ layer progenitor cell adhesion and cell size **(a)**  $F_{max}$  of homotypic progenitor cell adhesion as a function of contact time displayed as box-whisker plots. Median in black and mean in white. Numbers above/below brackets indicate  $p$  values for the corresponding combinations. **(b)** Distribution of  $F_{max}$  for the three progenitor cell types at 10 s contact time. Unprocessed raw data; binning set to 500 pN. **(c)** Box-whisker plot of the cell diameter for different progenitor cell types. Numbers above/below brackets indicate  $p$  values for the corresponding combinations. Phase contrast micrographs of typical progenitor cell morphology used in the SCFC experiments are shown above the box-whisker plots. Scale bar: 10  $\mu\text{m}$ . **(d-f)**

Involvement of Cadherin and Myosin in progenitor cell adhesion. **(d)**  $F_{max}$  as a function of contact time for progenitor cell adhesion to an E-cadherin-coated surface. **(e)** Intensity profile of E-cadherin staining in the hypoblast (mesoderm and endoderm progenitors) and epiblast (ectoderm progenitors) determined from Fig. 1f. E-cadherin plasma membrane intensities are higher in cells of the anterior axial hypoblast compared to adjacent epiblast cells. **(f)** Quantification of  $F_{max}$  for homotypic adhesion as a function of germ layer progenitor cell type in the presence or absence of Blebbistatin at 10 s contact time. Actual  $p$ -values are given above the brackets, number of observations below the whiskers.

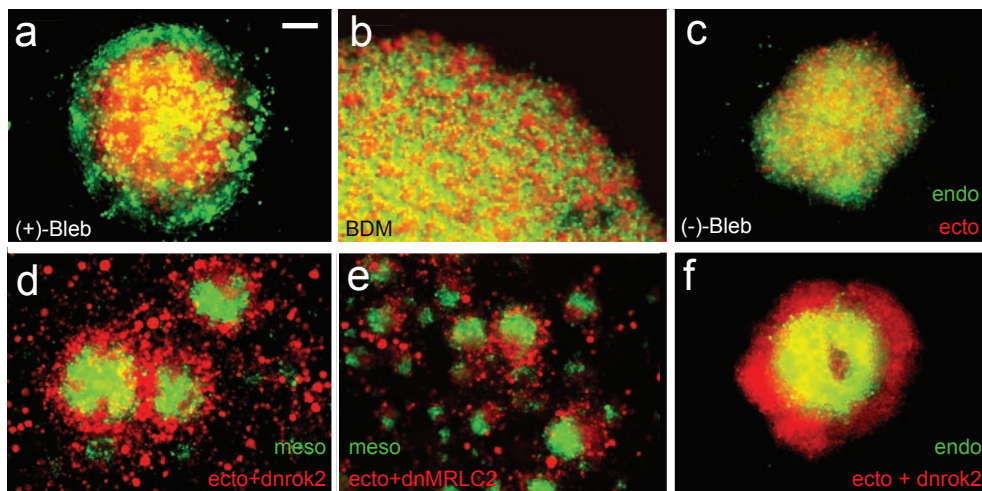


**Figure S3** Germ layer progenitor cell sorting and cortex tension. **(a,b)** Sorting in mesoderm (green) and ectoderm (red) hanging drop co-cultures in the presence of 50  $\mu$ M (+)-Blebbistatin **(a)** and 20mM BDM **(b)** after 17 h in culture. **(c)** Sorting of ectoderm (red) and endoderm (green) in hanging drop co-cultures in the presence of (-)-Blebbistatin after 17 h in culture. **(d-f)**

Sorting in mesoderm-ectoderm **(d,e)** and endoderm-ectoderm **(f)** hanging drop co-cultures with ectoderm cells (red) expressing either *dnrok2* mRNA **(d,f; 350 pg/embryo)** or *dnmrlc2a* mRNA **(e; 250 pg/embryo)** to reduce cortex tension after 17 h in culture. Scale bar in **(a)**=150  $\mu$ m. Images were constructed in ImageJ.

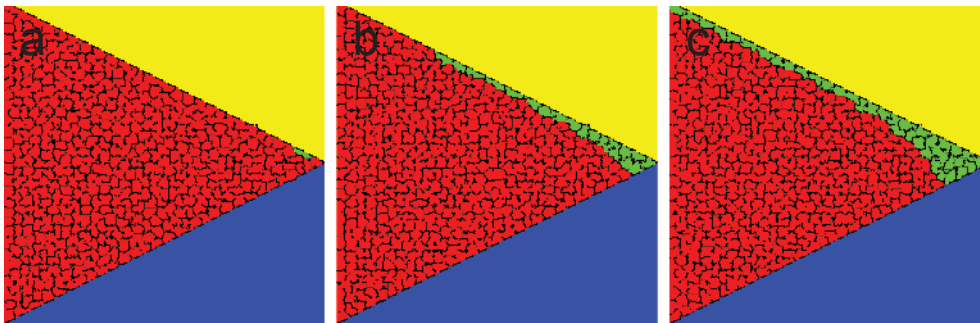


**Figure S4** Simulation of germ layer progenitor cell sorting in the presence of extra-embryonic EVL and yolk cell. Adhesion and tension values for mesoderm and ectoderm progenitors were set as in Fig.4. We further assumed that EVL cells adhere preferentially to ectoderm progenitors ( $J_{evl,ecto} > J_{evl,meso}$ ), that yolk and EVL cells do have uniform contraction (not interface-specific) and that the adhesion between yolk and the germ layer progenitors is equal to the homotypic adhesion of germ layer

progenitors ( $J_{yolk,meso} = J_{meso,meso}$ ,  $J_{yolk,ecto} = J_{ecto,ecto}$ ). **(a-c)** Simulation of consecutive steps of progenitor cell sorting at the germ ring margin with the yolk (yellow) and EVL (blue) positions fixed, the space between yolk and EVL filled with ectoderm cells (red), and the rightmost ectoderm cell differentiating into a mesoderm cell (green) at regular intervals. Similar to the situation at the germ ring margin, mesoderm progenitors disperse between the ectoderm and yolk.

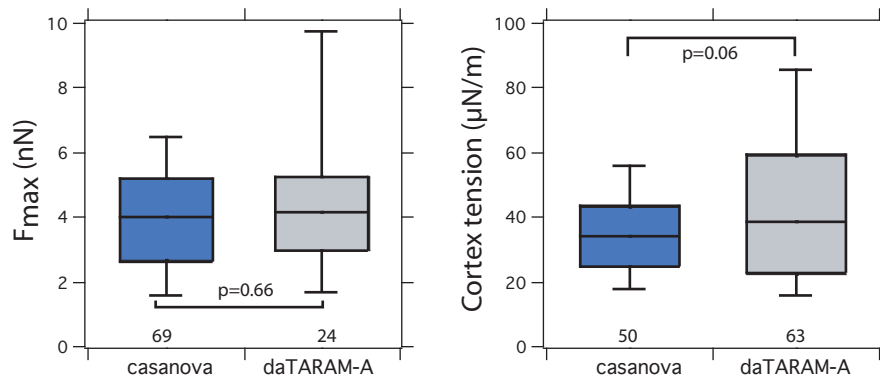


**Figure S5** Endoderm progenitor cell adhesion and tension.  $F_{max}$  for homotypic adhesion (a) and cortex tension (b) of endoderm cells obtained by expressing either *cas* mRNA (50 pg/embryo) or dominant

active *TARAM-A* mRNA (*daTARAM-A*; 50 pg/embryo). Actual *p*-values are given above/below the brackets, number of observations below the whiskers.

## Supplementary Methods

### *Embryo maintenance*

Fish maintenance and embryo collection was carried out as previously described<sup>1</sup>.

### *Primary cell culture*

For cell culture, dome-stage embryos (5 hpf) were dechorionated in 2 mg/mL Pronase (Roche) and transferred into dissociation medium (DMEM/F-12 + 0.5 mg/mL EDTA). The blastoderm was dissociated by gentle mixing to obtain single cells. Yolk remnants were removed by sedimentation in cell culture medium. The dissociation medium was replaced after centrifugation with CO<sub>2</sub>-independent DMEM/F-12+Pen/Strep for SCFS and cortex tension measurements, or DMEM+Pen/Strep for hanging drops and tissue explants.

### *Single-cell force spectroscopy (SCFS) set-up*

Cell-cell adhesion and cell cortex tension measurements were conducted with an AFM (Nanowizard I<sup>®</sup>, JPK Instruments) mounted on an inverted fluorescence microscope (Zeiss Axiovert 200, equipped with 20x and 40x lenses). Either phase-contrast or fluorescence imaging were used to select cells and monitor their morphology during force measurements (see below). The setup was extended with a JPK CellHesion<sup>®</sup> module to increase the cell-cell separation distance up to 100 μm and used in closed height feedback mode<sup>2</sup>. Cantilevers were calibrated *in-situ* using the thermal noise method<sup>3</sup> prior to experiments. The calibration procedure for each cantilever was repeated three times to rule out possible errors. Spring constants were found to be consistent with the manufacturer's nominal value (Veeco Instruments).

### *Statistical analysis*

After determining  $F_{max}$  for each force-distance curve, we averaged  $F_{max}$  over the experimental repetitions (see above) to determine the mean adhesion force of a given cell couple and contact time. The resulting values were then pooled to obtain the distribution of adhesion forces for a given experimental condition. The median±MAD (median

absolute deviation,  $MAD = median(x_i - \tilde{x})$  and percentiles were then extracted with a custom IgorPro (WaveMetrics) function and used in KaleidaGraph (SynergySoftware) for unpaired Wilcoxon based Mann-Whitney U-tests for significance with a  $p$  cut-off value of 0.05. Exact  $p$  values are given within the figures and were calculated using ' $R$ '. Non-parametric tests were used on all data, because we assumed that the data are not normally distributed. Although no systematic history effect on successive force-distance curves taken with one cell was detected (data not shown), we could not assume that each curve is strictly independent of each other. Furthermore, adhesion force data are likely to be dependent on different properties, e.g. more than one type of adhesion molecule, which does not allow us to use parametric tests. Wilcoxon based Mann-Whitney U-tests are distribution independent and can therefore be applied on composite data-sets. Box-whisker plots are presented with the box containing 50 % of the data around the median and whiskers encompassing 80 % of the data values. Pearson's rank correlation coefficient  $R$  was computed using IgorPro. Values of  $T_c$  for each test were pooled and tested using the same procedure.

#### *Cell aggregation experiment*

Hanging drop experiments were performed as described<sup>5</sup>. In short, embryos at the one-cell-stage were injected with a mix of fluorescently labeled dextran and *mRNAs* to induce homogenic cell fate in the embryo. After blastoderm dissociation at dome-stage (5 hpf),  $1.5 \cdot 10^6$  cells/mL of two different germ layer progenitor cell types were allowed to aggregate in 25  $\mu$ L or 50  $\mu$ L hanging drops. The ratio of co-cultured cells was set to 1:1 or 1:2 with the enveloping cell type at the higher concentration. Cultures were incubated for at least 17 h in a humidified chamber equilibrated with 5 %  $CO_2$  at 27°C. To reduce cortex tension, the cells were cultured in the presence of 50  $\mu$ M (-)-Blebbistatin (CalBioChem), 10 mM Cytochalasin D (Sigma) or 20 mM 2,3-butanedionemoxime (BDM, CalBioChem). Control aggregates were cultured in the presence of 50  $\mu$ M (+)-Blebbistatin (CalBioChem, Fig.S3a). Incubation in 5 mM EDTA did not lead to sorting (data not shown). To selectively inhibit cortex tension in ectoderm progenitors, *MZ-oepr* embryos were injected with 350 pg *dnrok2* *mRNA*. Images were taken after 0, 4, 6, 8 and 17 h in culture with Metamorph (Digital Imaging) using an epifluorescence microscope

(Zeiss Axiovert 200M equipped with EXFO X-cite 120, 5x lens, 470[40]BP/525[50]BP and 546[12]BP/575LP excitation/emission filters) and a CoolSnap CCD camera (Roper Scientific, 4.6x4.6  $\mu\text{m}^2$ , 12 bit pixel). Linear contrast adjustment was applied to the whole image using ImageJ. To analyze the sorting dynamics, 5000 cells of each type were cultured in a passivated micro-chamber. Sorting was followed with a rate of 4 frames/min and analyzed as described below. Culture in EDTA did not lead to any changes in cluster size (Fig.3h).

### *Image analysis*

To extract information about dynamic changes in boundary length or projected particle area during cell sorting, standard plug-ins for ImageJ were used. Images were first ‘binarized’ and ‘despeckled’ to remove single pixels in each frame, followed by ‘erode’ and ‘dilate’ steps. The number of particles was then counted, the area measured and normalized to the number of particles. Western blots were quantified using ImageJ. The average intensity of each single band was measured using equal sized boxes, background was subtracted and then normalized to the intensity of intracellular  $\alpha$ -tubulin. Confocal images of the transplanted embryos were analyzed using ImageJ. The perimeter of the embryo was fitted to a circle and the integrated radial intensity profile was calculated (intensity as a function of the center distance). The corresponding intensity values and distances were normalized and the mean intensity at a given position was calculated. Embryonic shield sections stained for E-cadherin were quantified using ImageJ. Cell boundaries were traced and staining intensity plotted against the distance to the shield.

### *Whole-mount antibody staining and cell surface biotinylation*

Whole-mount E-cadherin antibody staining on sections of gastrula stage embryos were performed as previously described<sup>1</sup>. For surface biotinylation experiments, dome-stage embryos (5 hpf) were dissociated in 1/2 Ringer solution w/o  $\text{Ca}^{2+}$  and washed three times in 1/2 Ringer.  $5 \times 10^6$  cells were incubated at 4°C in 1 mg/mL Sulfo-NHS-biotin in PBS (Pierce Biotechnology, Cell surface biotinylation kit). After 30 min the reaction was quenched and the cells were washed twice in TBS. To separate biotinylated proteins from the intracellular pool, the manufacturer’s protocol was followed. Total protein content

was estimated using a BCA test (Pierce Biotechnology). For Western blotting, equal amounts of mesoderm, endoderm and ectoderm membrane fraction were transferred onto a 10 % polyacrylamide gel. Classical cadherins were detected using a rabbit anti-pan-cadherin antibody (1:5000<sup>6</sup>) and a HRP-coupled secondary donkey anti-rabbit (1:2000, Amersham Bioscience). As loading controls a mouse  $\alpha$ -tubulin antibody (Sigma, 1:2000) was used. Secondary antibody detection was done using a chemiluminescent substrate kit (1:1 ECL kit, Amersham Bioscience) and detected in a FujiFilm LAS 3000 imagereader.

#### *In situ hybridizations*

Whole mount *in-situ* hybridization were performed as described previously<sup>1</sup>. For *gsc*-, *ntl*-, *gata2*- and *sox17*- *in-situs*, antisense RNA probes were synthesized from partial sequences of the respective cDNAs. Pictures were taken with a dissecting scope (Olympus SZX 12) equipped with QImaging Micropublisher 5.0 camera.

#### *Cell transplantations*

Cell transplantations were carried out as described<sup>1</sup>. In short, cells from donors fluorescently labeled with FITC- or TRITC- dextran (Molecular Probes) were transplanted into *MZ-oep:ras-GFP* transgenic hosts at shield stage (6 hpf) and fixed in 4 % paraformaldehyde at bud stage (10 hpf). Optical 3D sections were acquired with an upright Leica SP5 confocal microscope equipped with a 20x water immersion lens using 488 Argon and 633 HeNe laser lines.

#### *Germ layer explants*

Tissue explants followed by Phalloidin staining were carried out as previously described<sup>5</sup>. Pictures were taken with an Zeiss LSM Meta upright microscope using and 543 HeNe laser 542(12)BP excitation and 573LP emission filters.

#### *Numerical simulations*

The *Cellular-Potts-Model*<sup>7</sup> was used to perform simulations on a 2D square lattice, measuring 230x230 pixels. The algorithm for energy minimization is based on Monte Carlo sampling and the Metropolis algorithm (for a detailed description of the procedure

see <sup>7</sup>). An energy is assigned to each cell and interface, with the total energy of a cell aggregate as defined by<sup>8,9</sup>:

$$H = \sum_{\text{interfaces}} P_{ij}(C_{ij} + C_{ji} - J_{ij}) + \sum_{\text{cells}} \lambda_p (P_i - P_0)^2 + \sum_{\text{cells}} \lambda_A (A_i - A_0)^2$$

In this model the adhesion between the cell  $i$  and  $j$  is  $J_{ij}$  and the cortical tension of cell  $i$  at the interface with cell  $j$  is  $T_{ij} = C_{ij} + 2\lambda_p(P_i - P_0)$ . The interfacial tension between cell  $i$  and cell  $j$  is thus  $\gamma_{ij} = T_{ij} + T_{ji} - J_{ij}$ . Differential interfacial tension is modeled by assigning interface-specific values to  $C_{ij}$ .  $\lambda_p$  and  $\lambda_A$  are the perimeter and area moduli,  $P_0$  and  $A_0$  the target perimeter length and area of cell  $i$ . For the adhesion energies we chose  $J_{ecto,ecto}=200$ ,  $J_{endo,endo}=300$ ,  $J_{meso,meso}=400$ ,  $J_{ecto,endo}=J_{ecto,meso}=J_{meso,endo}=200$ , and  $J_{ecto,medium}=J_{meso,medium}=J_{endo,medium}=0$ . To qualitatively represent the differences in the cortical tensions of the cells, we used the following for the simulations in Fig. 4a-e:  $C_{ecto,medium}=300$  and  $C_{meso,medium}=50$  and for all other interfaces,  $C_{ij}=0$ . Other parameter values are  $\lambda_p=0.3$  and  $P_0 = \frac{(\sqrt{\pi A_0})}{10}$ ,  $\lambda_A=25$  and  $A_0=50$  for all cells with a fluctuation allowance  $T=300$ .

### Supplementary References:

1. Montero, J.A. *et al.* Shield formation at the onset of zebrafish gastrulation. *Development* 132, 1187-1198 (2005).
2. Puech, P.H., Poole, K., Knebel, D. & Muller, D.J. A new technical approach to quantify cell-cell adhesion forces by afm. *Ultramicroscopy* 106, 637-644 (2006).
3. Hutter, J.L. & Bechhoefer, J. Calibration of atomic force microscope tips. *Review Scientific Instruments* 64, 1868-1873 (1993).
4. R Development Core Team (R Foundation for Statistical Computing. Vienna, Austria, 2007).
5. Schötz, E.-M. *et al.* Quantitative differences in tissue surface tension influence zebrafish germ layer positioning *HFSP Journal* (in press).
6. Geiger, B. *et al.* Broad spectrum pan-cadherin antibodies, reactive with the c-terminal 24 amino acid residues of n-cadherin. *J Cell Sci* 97, 607-614. (1990).
7. Maresca, A.F.M., Grieneisen, V.A. & Hogeweg, P. The cellular potts model and biophysical properties of cells, tissues and morphogenesis. (Birkhäuser Verlag, Basel; 2007).
8. Ouchi, N.B., Glazier, J.A., Rieu, J.-P., Upadhyaya, A. & Sawada, Y. Improving the realism of the cellular potts model in simulations of biological cells. *Physica A: Statistical Mechanics and its Applications* 329, 451-458 (2003).

9. Kafer, J., Hayashi, T., Maree, A.F.M., Carthew, R.W. & Graner, F. Cell adhesion and cortex contractility determine cell patterning in the drosophila retina. *Proceedings of the National Academy of Sciences* 104, 18549-18554 (2007).